

Calibration, event reconstruction, data analysis and limits calculation for the LUX dark matter experiment

(LUX Collaboration)

(Dated: December 21, 2015)

abstract

I. INTRODUCTION – DAN M - LAST UPDATE 08-09-2015

The Lambda Cold Dark Matter (Λ CDM) model of the universe is in excellent accord with multiple types of astrophysical observations [1, 2]. According to the most recent results from Planck, the mass/energy content of the universe is made up of 26.8% cold dark matter (CDM), nearly 5.5 times larger than the 4.9% component due to baryonic matter [3]. The identity of the CDM is unknown, but a number of theoretical models predict that dark matter particles interact very weakly with ordinary matter. Such models include weakly interacting massive particles [4, 5] and asymmetric dark matter [6, 7], and in either case, predict that dark matter particles can elastically scatter off nuclei, producing nuclear recoils with energy of order 1-100 keV. Such elastic scattering events could be detectable using sufficiently sensitive instruments. A positive direct detection of dark matter interactions would open a window into physics beyond the Standard Model, give new insights in cosmology, and create a new field of direct dark matter observations.

One of the most effective technologies for the direct detection of dark matter is the two-phase Xenon Time Projection Chamber (Xe TPC) [8–12]. Xenon is low in intrinsic backgrounds since it has no long-lived isotopes other than the extremely long-lived ^{136}Xe isotope, which undergoes double beta decay with a half-life of 2.1×10^{21} years [13, 14] and, at the low energies relevant to WIMP detection, produces a background that is small in comparison to the electron scattering of solar neutrinos [15]. Liquid xenon is dense (2.9 g cm^{-3}), and produces large scintillation and charge signals from both electron recoil (ER) and nuclear recoil (NR) events. The Xe TPC has the ability to discriminate ER and NR on an event-by-event basis using the charge-to-light ratio, and can be expanded to large, homogenous volumes. With excellent position resolution and short LXe gamma ray and neutron scattering lengths, this technology allows excellent self-shielding and extremely low backgrounds at low energies.

The Large Underground Xenon (LUX) experiment [11] is the most recent two-phase Xe dark-matter detector to begin operations, and in its most recent result [16] it has achieved world-leading WIMP sensitivity for WIMP masses above $3.5 \text{ GeV}/c^2$, reaching a minimum spin-independent WIMP-nucleon cross section limit of $3 \times 10^{-46} \text{ cm}^2$ at $33 \text{ GeV}/c^2$. LUX is located at the 4850 ft. level of the Sanford Underground Research Facility (SURF) [17] in Lead, South Dakota. LUX was assembled and first operated in a dedicated surface facility at SURF

starting in 2009. A followup test of LUX on the surface (Run 2) started in October 2011 and ended in February 2012 [18]. The Davis Campus, 4850 ft underground, was built to house LUX and other experiments, and completed at the end of May 2012. LUX began installation in the Davis Campus in June 2012 and the cooldown of the detector began in January 2013. The first WIMP search and calibration data (Run 3) were acquired during the period March–October 2013. First results from Run 3 were announced in October 2013 and subsequently published in Physical Review Letters [19]. After further calibration studies, re-analysis of Run 3 data has recently been announced [16]. Data collection continues, with the completion of a 300 live-day WIMP search (Run 4) expected in 2016.

II. THE LUX EXPERIMENT – DAN M - LAST UPDATE 08-09-2015

LUX is a two-phase Xe TPC designed to detect the prompt scintillation light and ionization electrons due to ionizing radiation. A schematic of the LUX detector is shown in Figure 1, and photographs of LUX without its inner vessel, within the time projection chamber, and mounted in its water tank shielding, is shown in Figures 2, 3, and 4.

The central, fully active Xe region is defined by 12 PTFE reflector panels, the gate grid located 0.5 cm below the Xe liquid surface, and the cathode grid located 48 cm below the gate grid. The maximum width is 47 cm. Field shaping rings, spaced by 2 cm, are mounted on the outer PTFE vessel, and apply an electric field to drift the ionization electrons. An anode grid 0.5 cm above the surface, and a gate grid 0.5 cm below the surface, are used to generate high fields that extract the electrons and accelerate them, thus generating proportional scintillation light. Scintillation photons are produced almost uniformly along the gas gap, regardless of the electron extraction location. In Run 3, the LUX detector was operated with cathode, gate, and anode voltages of -10.0 kV, -1.5, and +3.5 kV respectively, corresponding to an average drift field of 180 V/cm and an electron extraction field of 6.0 kV/cm applied in the gas (3.1 kV/cm in the liquid).

An event in the LUX time projection chamber is characterized by two signals, corresponding to detection of direct scintillation light (S1) and proportional light from ionization electrons (S2). The two light pulses occur within the maximum drift time of 320 microseconds, for a saturated electron drift velocity of 1.51 mm/microsecond

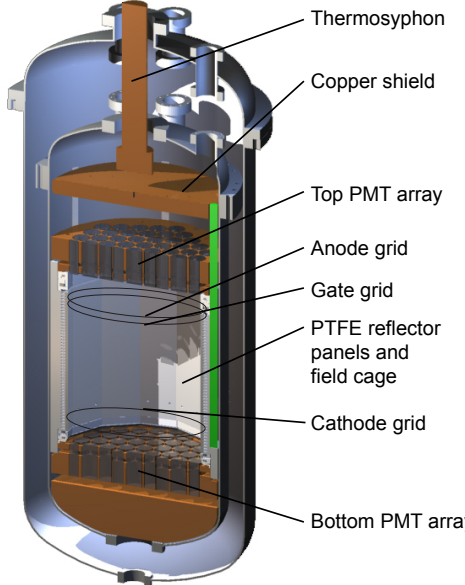


FIG. 1. Schematic of the LUX detector. LUX is a two-phase xenon time projection chamber containing 250 kg of active LXe mass viewed from above and below by PMT arrays.



FIG. 2. Photograph of the LUX detector, with inner can removed.

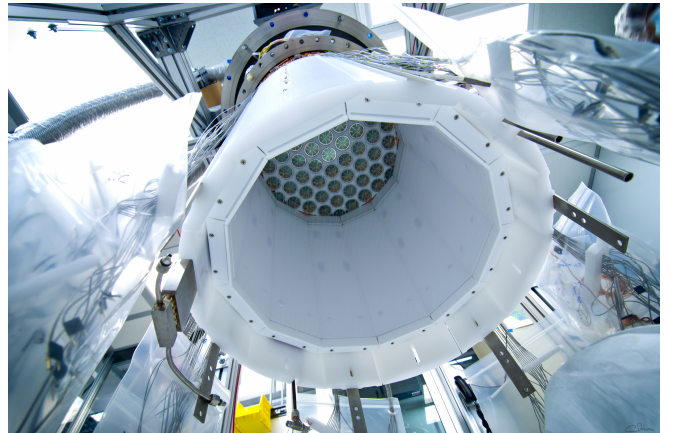


FIG. 3. Photograph of the inside of the LUX detector, with lower PMT array removed.



FIG. 4. Photograph of LUX installed in the Davis Cavern water shield at SURF.

in LXe. Since electron diffusion in LXe is small, the S2 proportional scintillation pulse is produced in a small spot. After corrections for any field-non-uniformities, the original event may be located accurately in x-y, allowing 2D reconstruction. With precise z information from the drift time measurement, the 3D event localization provides background discrimination via fiducial volume cuts.

Two arrays of 5 cm diameter R8778 (Hamamatsu) photomultiplier tubes (PMTs), 61 in each array, detect the S1 and S2 signals. One PMT array above the liquid surface is primarily used to image the x-y position of the proportional light pulse. The second PMT array is in the liquid, below the cathode grid. Because of internal reflection at the liquid surface (LXe has a high refraction index of 1.69 at 170 K) most prompt light is collected in this bottom array. Because of the high quantum efficiency of the R8778, highly transparent grids, and use of PTFE reflectors between PMTs, very high light yield is achieved (8.8 photoelectrons/keV electron-equivalent energy for 122 keV γ -rays at zero electric field).

LUX has introduced a number of innovations, including a low-radioactivity titanium cryostat, nitrogen thermosyphons, high-flow Xe purification, two-phase Xe heat exchangers, internal calibration with gaseous sources of ^{83m}Kr and ^3H , and nuclear recoil calibration using multiple scatters of monoenergetic neutrons produced with a DD generator. The LUX cryostat vessels were fabricated from Ti with very low levels of radioactivity [20], rivaling even Cu. The two-phase TPC technique requires

precise control of the thermodynamic environment, and this was achieved in LUX through the development of an innovative system of nitrogen thermosyphons. These feature precise, tunable, automated control of cooling up to hundreds of kW, plus stable and reliable remote operation. Among other things, this system has allowed highly controlled initial cooling power of the system [11], which is necessary to avoid warping of the large plastic structures of the TPC. A related development is the purification system that allows rapid circulation of Xe through an external gas-phase getter at flows exceeding 27 standard liters per minute (229 kg/day), while maintaining a stable liquid surface through the use of a weir. Using a two-phase heat exchanger system [21] and very efficient heat transfer between evaporating and condensing Xe streams, negligible overall heat load on the detector is obtained. Xe purification was greatly aided by the use of an innovative gas trapping and mass spectrometry system [22, 23] that is sensitive to impurities at the sub-ppb concentration needed for good electron transport and light collection. This diagnostic capability₁₈₈ allowed various portions of the gas system and detector to be monitored for contamination. Removal of Kr₁₉₀ from the Xe, so as to limit ⁸⁵Kr ⁸¹Kr beta-decay back-₁₉₁ grounds, was performed before Run 3 using a charcoal₁₉₂ column. These systems were demonstrated during LUX₁₉₃ first science run, where cooldown was achieved in only₁₉₄ nine days. Sufficient purity to begin science operations,₁₉₅ corresponding to an electron drift lifetime of over 500 μ s,₁₉₆ was achieved only 1 month after the initial filling with₁₉₇ LXe. We achieved stable operation of the detector with₁₉₈ mostly unattended operation over the five-month period,₁₉₉ during which the pressure and liquid level had sufficient₂₀₀ stability (1% and < 500 μ m, respectively) to introduce₂₀₁ no measurable variations in the S2 or S1 signals.₂₀₂

203
204
205
206
207
208
209
210

169 III. DATA ACQUISITION AND REDUCTION

170 A. DAQ configuration and single photoelectron 171 digitization acceptance – Carlos - Last update 172 09-10-2015 (FW)

173 The signal at each PMT output is amplified by 5 with₂₁₁
174 a linear pre-amplifier at the instrumentation breakout₂₁₂
175 and is subsequently shaped by a post-amplifier that in-₂₁₃
creases the pulse area by 1.5. The post-amplifier boards₂₁₄
have additional amplification outputs to feed the LUX₂₁₅
trigger and discriminator boards. The output of the₂₁₆
post-amplifier is digitized by 14-bit Struck SIS3301 ADC₂₁₇
boards at a sampling rate of 100 MS/s (10 ns data sam-₂₁₈
ples). The Struck board firmware was modified to use₂₁₉
pulse-only digitization (POD), a zero-suppression mode₂₂₀
that only digitizes signals above a specified threshold.₂₂₁
Since signals in LUX are dominated by long periods of₂₂₂
baseline with short bursts of S1 (width < 100 ns) and S2₂₂₃
(width < 5 μ s) signals, POD mode significantly reduces₂₂₄
the number of recorded samples while increasing the₂₂₅

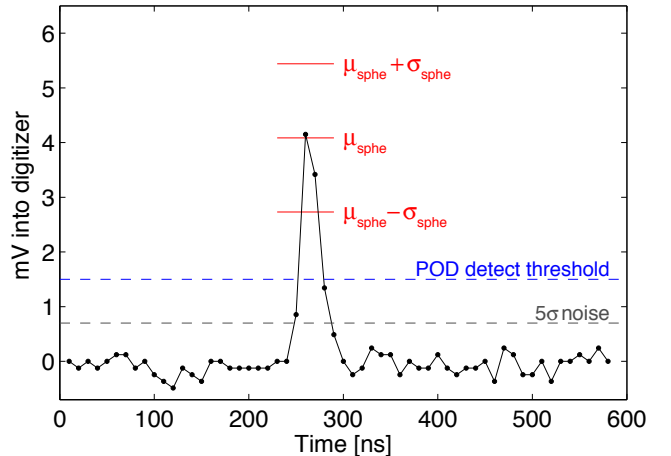


FIG. 5. Threshold diagram

maximum allowed acquisition rate. The signal threshold to begin digitizing the PMT signal was set to 1.5 mV at the Struck input; the signal threshold to end digitizing was set to 0.5 mV. An additional 24 samples before and 31 samples after the threshold crossings are also digitized. The LUX analog signal chain and DAQ maintain linearity in S1 and S2 signals at energies of \sim 100 keV_{ee}, orders of magnitude above the WIMP region of interest and comfortably above the ⁸³Kr and tritium ER calibrations. For a more detailed description of the LUX DAQ system, refer to Ref. [24].

PMT signals are continuously recorded by the DAQ regardless of trigger conditions and the trigger pulse is digitized as an additional DAQ channel. Offline software called the Event Builder subsequently matches PMT signals within a specified time window around the trigger pulse for data processing and analysis. In this way, trigger changes can be made offline with no data loss.

For the nominal PMT gains of 4×10^6 , the single photoelectron (sphe)

is 4 mV with a full width at half max (FWHM) of about 20 ns. A typical sphe pulse is shown in Fig. 5 with height markers for the mean sphe height (μ_{sphe}) and its standard deviation ($\mu_{\text{sphe}} \pm \sigma_{\text{sphe}}$). The total noise from the electronics chain and the ADC, as measured at the Struck input, is 155 μ V_{rms}. The 1.5 mV POD threshold is indicated, as well as the height of a 5 σ noise fluctuation.

In order to estimate the single photoelectron digitization acceptance η_{sphe} for each PMT, a Gaussian distribution fit truncated at the POD threshold of 1.5 mV was performed on the single photoelectron spectrum. Note that this single photoelectron calibration was performed with 400 nm light pulses from the LED calibration system, which does not account for double photoelectron emission. Therefore, the quoted numbers here are conservative since that effect would result in a very modest increase in η_{sphe} . Fig. 6 shows an example distribution with $\eta_{\text{sphe}} \sim 0.95$. The distribution of η_{sphe} values for the

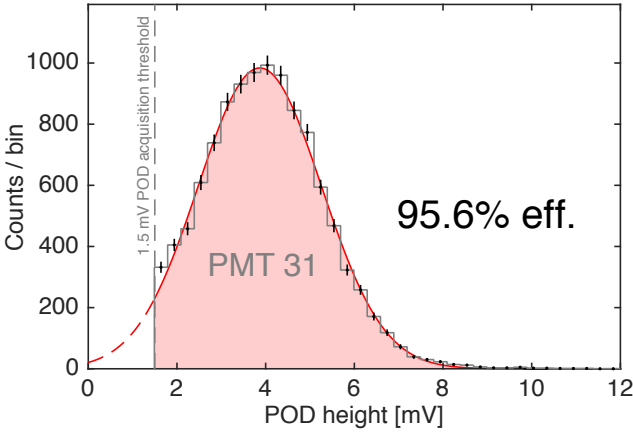


FIG. 6. Measured maximum single photoelectron pulse height for PMT 31. The 1.5 mV POD threshold is indicated by the vertical dashed line. Based on a fit of the single photo electron pulse height distribution, it is estimated that 95.6% of the single photoelectrons in PMT 31 produce a pulse that exceeds the POD threshold.

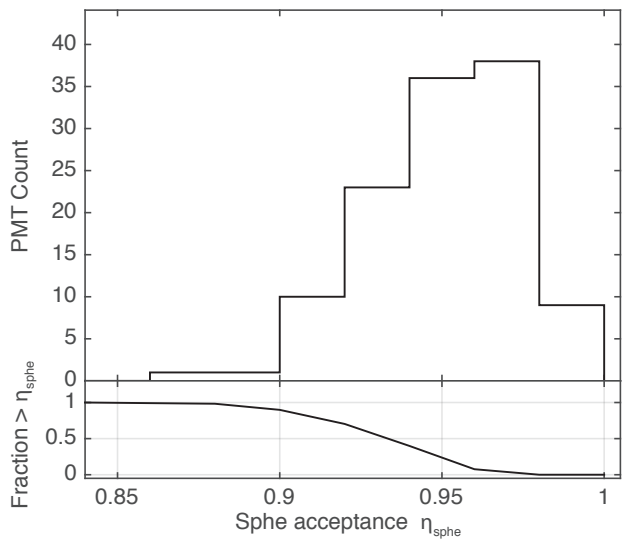


FIG. 7. Single photoelectron acceptance distribution for all 122 photomultiplier tubes

are summed into 16 trigger channels, with no adjacent PMTs belonging to the same sum. The sums are individually processed using two eight channel DDC-8DSP digitizers/processors that communicate with a common Trigger Builder to make a final trigger decision. Internal digital filters perform baseline subtraction and signal integration. In Run 3 the trigger required that at least two of these channels have a signal greater than 8 phe within a $2 \mu\text{s}$ window. The overall trigger efficiency has a strong dependency on the required 2-fold coincidence and reaches $>99\%$ efficiency for S2 signals with a total area of 100 phe. Detailed study of the trigger efficiency is discussed in [26]. For the first third of run the hold-off time was set to 4 ms. Analysis of the data being collected showed that the hold-off period does not have to be this long and subsequently was set to 1 ms for the remainder of the run. This improved the live-time slightly and was verified to have no negative impact on the overall results.

C. The LUX data processing framework – Carlos - Last update 07-31-2015 by Alex

The LUX data processing framework (DPF) is a flexible, modular and multi-language framework developed by the LUX collaboration for extracting the relevant features from the raw digitized PMT data and outputting a set of reduced quantities (RQs) that can be used for physics analyses. The LUX DPF employs interchangeable algorithm modules with standardized inputs and outputs that perform predefined tasks, such as calibration, pulse finding, classification and interaction vertex position reconstruction. These algorithm modules can be written in any supported programming language, which currently include C++/ROOT, Python and MATLAB. A MySQL database (referred to as the “LUG”) stores version-controlled calibration values and correction maps, data processing input settings and data processing logging, among other bookkeeping values. The LUX DPF was written entirely in Python and can be executed on computing clusters, and desktop and laptop computers (provided they have network access permissions to the LUG database). The list of modules to use, their order and specific configuration (e.g. threshold value for a pulse finder algorithm) and required calibration constants must be provided to the framework in an input settings file in XML format – which is stored in the LUG database and associated with a unique identifier (called global settings number). This identifier allows the collaboration to easily establish the exact conditions used to process any dataset and ensures that all the data used in a particular analysis campaign is processed with the same settings.

The Event Builder reads the raw data as digitized by the DAQ and extracts the portions that are located in a time window before ($\Delta t_{\text{pretrigger}}$) and after ($\Delta t_{\text{posttrigger}}$) the trigger pulse (which is also a digitized waveform in a separate channel). This window is referred to as an

PMTs used during Run03 is shown in Fig. 7. All but two PMTs had a single photoelectron digitization acceptance greater than 0.90; the mode of the distribution is above 0.95.

B. Trigger – Eryk - Last update 08-24-2015

The LUX trigger system is described in detail in [25]. It is a digital FPGA-based system that flags events in the DAQ data stream for further analysis. All 122 PMTs

“event”. For Run03, both $\Delta t_{\text{pretrigger}}$ and $\Delta t_{\text{posttrigger}} = 0.5 \text{ ms}$. Given that the maximum Run03 electron drift time was $324 \mu\text{s}$, these values ensure that both the S1 and the S2 pulses are contained in every event since either pulse type may induce a trigger.

The settings used in the Event Builder are stored in the LUG database, and the output file set is assigned a unique identifier that corresponds with the LUG record. The output of the Event Builder is read by the LUX DPF modules.

The LUG database, in addition to storing data processing bookkeeping values (such as the Event Builder settings, DPF global settings and details about each individual data processing run) also stores calibration constants for the detector. These calibration constants include PMT gains, x,y,z spatial calibration maps for S1 and S2 pulses, the electron lifetime, detector tilt measurements, light response functions for position reconstruction, and energy calibration parameters, among others. These are sent to each data processing run as specified in the XML settings file for access by the algorithm modules. The calibration constants stored in the LUG are stored with submission dates, version numbers, originating dataset name (from which the values were calculated) and algorithm names. The latter allows for different methods of obtaining a calibration parameter to be selected during a data processing run.

316 D. Data processing algorithms

317 1. Pulse finder and classifier – Cham - Last update 318 08-04-2015

319 At the heart of a reduced quantities based analysis
320 stands a pulse finding algorithm searching for valid³⁴³
321 pulses in the acquired waveforms to be stored for further³⁴⁴
322 analysis. Any detected pulses are subsequently classified³⁴⁵
323 according to their shape and properties. This section³⁴⁶
324 describes the pulse identification modules, including the³⁴⁷
325 pulse finder and pulse classifier, used for the analysis of³⁴⁸
326 the first WIMP search run data taken by LUX.³⁴⁹

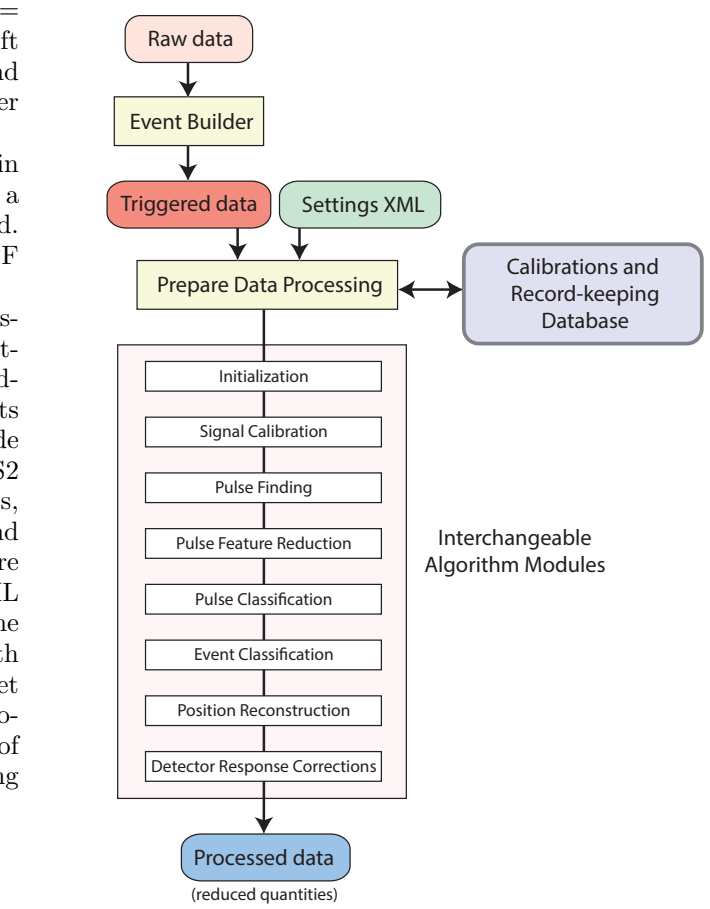


FIG. 8. The LUX Data Processing Framework

327 the maximum amplitude in the boxcar. The start and
328 end times of the pulses are set at the point where
329 the smoothed waveforms stay below the set baseline
330 noise threshold of 0.1 detected photoelectrons (phd)
331 per sample for a time of $0.5 \mu\text{s}$. In addition, valid pulses need
332 to be at least 30 ns (3 samples) wide or their average
333 amplitude must exceed the baseline noise threshold.
334 If the pulse width exceeds $6 \mu\text{s}$, a moving average filter
335 with a larger width parameter (250 ns) is used, moving
336 forwards and subsequently backwards in time from
337 the point of maximum amplitude in the waveform.
338 If a falling edge is followed by a continuous rise in amplitude
339 for a minimum of $0.5 \mu\text{s}$, this filter allows identification
340 of possible additional signal clustered with the original
341 pulse. If two or more individual signals are found the
342 algorithm splits the original waveform and stores only
343 the start and end time of the largest of the two pulses.
344 Finally, if a pulse has been found the corresponding
345 amplitude in the waveform is set to zero and all of the
346 steps described above repeated until all pulses in the
347 waveform, up to a maximum of 10, have been identified.

348 We minimise the possibility of missing small S1 signals

349 The pulse finder is based on a sliding boxcar filter³⁶¹
350 (width of $4 \mu\text{s}$), passing over the full event waveform³⁶²
351 for each triggered event and finding the region that³⁶³
352 maximises the enclosed area. A moving average filter³⁶⁴
353 (30 ns width) smooths the regions left and right from³⁶⁵

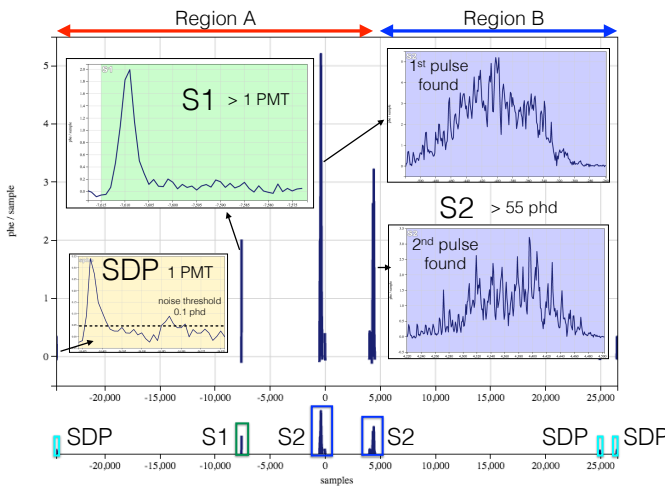


FIG. 9. Example double scatter event waveform. The search regions are labeled A and B, with the first, A, prioritized. Additionally to the main signal, this event contains three single detected photons (SDPs), with one shown as an inset to indicate the noise threshold of the pulse finder.

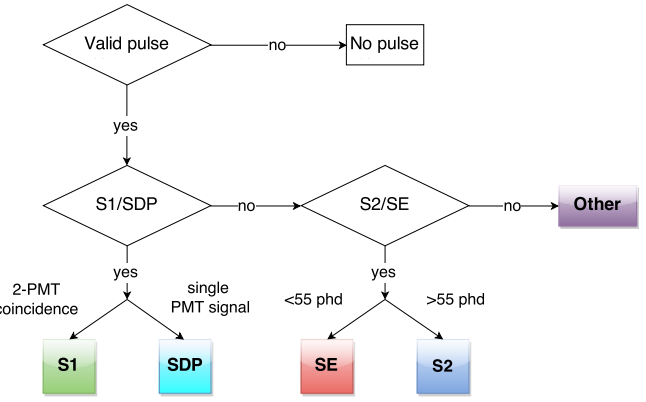


FIG. 10. Pulse classification decision tree.

S1 in comparison to an S2-type signal, utilising the ratio between two boxcar filters of length $0.5\ \mu\text{s}$ and $2\ \mu\text{s}$; pulse rise time, based on width ratios and area fractions, using the distinct shape of an S1 like signal from scintillation that features a sharp rise at the pulse start in comparison to the rather symmetrical S2-like signals from electroluminescence in the gas; PMT hit-distribution, where S1 signals are predominately recorded by the bottom PMT array due to total internal reflections off of the liquid-gas interface and the geometry of the TPC. For the assignment of an S1 signal two additional requirements have to be met. First, to reject pulses that are composed solely of baseline fluctuations, the maximum amplitude per sample within the full length of a pulse for at least 2 individual PMTs must exceed a $0.09\ \text{phd}/\text{sample}$ amplitude threshold. Second, a 2-PMT coincidence requirement is imposed to reject designation of single detected photons from spontaneous PMT photocathode emission as S1-signal. The 2-PMT coincidence interval is set to 10 samples in width since we expect $\sim 80\%$ of the S1 signal for over 90% of both ER and NR pulses to arrive within 100 ns. The 2-PMT coincidence requirement must be satisfied by at least two non-partnered PMTs each exceeding a $0.3\ \text{phd}$ integrated area threshold. SE- and S2-type signals are separated in energy. A valid S2 signal must exceed $55\ \text{phd}$ in size (corresponding to ~ 2.5 electrons). Those pulses that fall below this threshold are classified as SEs as long as their area is greater than $5\ \text{phd}$.

2. Event classification – Cham - Last update 08-04-2015

The event type of interest for the WIMP search analysis is a single scatter, or “golden”, event. The definition and procedure for the selection of golden events is as follows:

- There is only one valid S2 signal in the event after a valid S1 (S2s before the selected S1 are allowed).
- There is only one valid S1 signal before the selected

in the presence of single electrons, PMT afterpulsing, or other spurious signals, by using a complementary search logic that takes advantage of the preponderance for such pulses to dominate the region of the waveform following a large S2 signal. After the first two pulses have been found, where these are the two largest pulses in the waveform and ensure identification of multiple scatters, the waveform is split into two search regions of differing priorities. The region before the pulse that occurred at the later time in the waveform is scanned first with the standard boxcar filter algorithm. If the maximum allowed number of pulses has not been reached after scanning this first search region the algorithm will continue to fill the empty slots with pulses from the second search region. Figure 9 shows an example waveform of a multiple scatter event, indicating the regions of the search logic. Once pulses have been identified, independent modules subsequently parameterise the pulses for further analysis and classification of signal types.

The pulse classification module assigns each identified pulse to one of the following five signal types according to the extracted pulse parameters: S1, S2, single detected photon (SDP), single electron (SE), and unclassified. The algorithm is represented by the decision tree diagram in Fig. 10. First, S2- and SE-like signal types are assigned followed by S1 and SDP type signals, ensuring that S1-like signals are not overwritten by S2-like ones. Events that fail all four previous categories are assigned an “unclassified” flag. The signal-type assignment is based on a number of pulse parameter as follows: a width selection, exploiting the much narrower width of an

436 S2 (S1s following the S2 signal are allowed).

- 437 • The area of the S2 pulse must be larger than the
438 area of the S1.

439 The purity of the golden events selected by the DPF
440 was evaluated through a detailed hand-scanning cam-
441 paign. From an AmBe NR calibration dataset (live-time
442 of 2.53 h) 4000 pre-selected events were categorised by
443 eye using only the raw waveforms without any informa-
444 tion from the reduced quantities. The pre-selection of
445 events (to $\sim 2\%$ of the dataset) is necessary to reduce the
446 number to be scanned and at the same time increase the
447 statistics for single scatter events in the region of inter-
448 est. The cuts for pre-selection are predominately based
449 on event information (number of non-empty samples in
450 an event and the full event area), utilising only very ba-
451 sic additional pulse parameters such as the largest pulse
452 found and if a clear sub-cathode event has been identified.
453 Of the 4000 pre-selected events of order 200 single scatter
454 events have been identified. These are then compared to
455 the result from the event classification DPF module. Ap-
456 plying all WIMP search analysis cuts (see section VI A),
457 the purity of genuine golden events selected by the DPF
458 was determined to be 98%.

459 *3. XY Position reconstruction – Carmen - Last update* 490
460 *08-11-2015* 491

492 iteration, the initial x-y positions are obtained using a
493 different and simpler method of position reconstruction
(e.g., weighted mean).

494 The x-y position of an interaction in the LUX detec-
495 tor is recovered directly from the observed S2 signal, by
496 looking at the distribution of pulse areas on the top pho-
497 tomultiplier array. The algorithm used for the x-y posi-
498 tion reconstruction is called Mercury, and is based on the
499 method developed for the ZEPLIN-III experiment in [27].
500 The algorithm is a statistical search for the x-y position
501 that matches the observed S2 pulse areas on the PMT
502 array to expected pulse areas. The expected PMTs sig-
503 nals are obtained using a pre-determined set of empirical
504 functions called light response functions (LRFs), which
505 describe the average response of each individual PMT as
506 a function of the interaction position. The major advan-
507 tage of the Mercury method is that it needs only mea-
508 sured data rather than simulations to recover the position
509 of interactions, and thus it can recover features from the
510 data that are not well simulated or that we are not aware
511 of a priori.

512 The LRFs for each PMT are obtained through an iter-
513 ative fit to experimental data, which in the case of Run
514 3 corresponds to the krypton calibration data. In each
515 iteration, new LRFs are obtained by fitting the response
516 of the individual PMTs as functions of the event posi-
517 tions. We feed these new functions into the position re-
518 construction program to get new improved position of
519 interactions, which are then used to find new improved
520 LRFs. This process is repeated several times until the
521 functions are stable and the distribution of the krypton
522 events is uniform in the chamber. For the first fitting

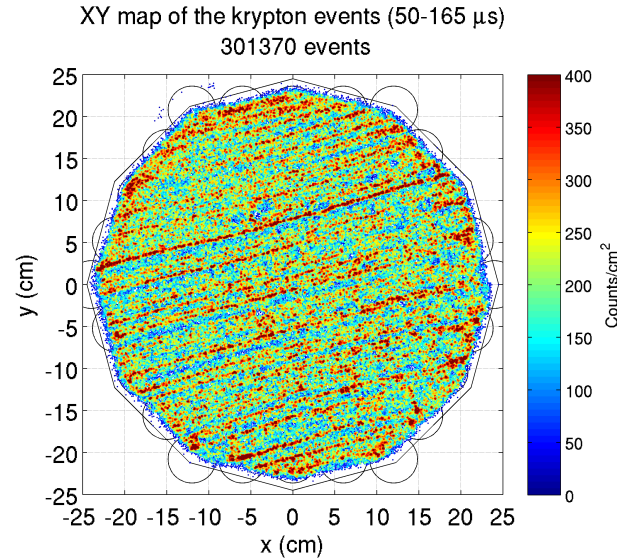


FIG. 11. XY map of the krypton events.

523 The simplest model for the LRFs consists of using ra-
524 dially symmetric functions that depends only on the dis-
525 tance d between the PMT and the event. Although this
526 model was successfully used in ZEPLIN-III, it cannot be
527 applied with satisfactory results in the LUX experiment.
528 Unlike the ZEPLIN-III detector, the inner walls of LUX
529 are covered with PTFE, which is a very good reflector
530 for the xenon scintillation light. This causes the amount
531 of reflected light to increase for events near the walls,
532 and requires a more complex model using 2-dimensional
533 functions for the PMT response. Thus, the LUX LRFs
534 are modeled as the sum of two components. The first
535 component describes the light that goes directly from
536 the interaction to the PMT and it depends only on the
537 distance between the event and the center of the PMT.
538 The second component corresponds to the light that is
539 reflected in the walls of the detector, and is described as
540 function of the event radial position and also the distance
541 between the event and the center of the PMT [28].

542 Figure 11 shows the final x-y distribution of events in
543 the krypton calibration dataset using the Mercury algo-
544 rithm. The observed stripped pattern is a consequence
545 of the geometry of the wires used to provide the electric
546 field. The pattern originates from a focusing effect of the
547 electrons near the gate wire region, caused by the differ-
548 ence between the fields in the drift region (180 ± 1 V/cm)
549 and in the liquid extraction region (2.76 ± 0.03 kV/cm).
550 This effect is a limiting factor for our resolution, and can
551 be used to assess the quality of the reconstruction.

522 4. *Estimators of light and charge – Alastair - Last update* 579
 523 *07-02-2015*

524 The light of WIMP-region-of-interest S1s, where the⁵⁸¹
 525 mean number of detected photons per channel is signifi-⁵⁸²
 526 cantly less than one, can be reconstructed with improved
 527 precision by using the count of candidate single-photon⁵⁸³
 528 pulses in individual PMT waveforms, termed 'spikes',⁵⁸⁴
 529 in addition to pulse areas: digital counting avoids vari-⁵⁸⁵
 530 ance that would arise from the inherent width of PMTs,⁵⁸⁶
 531 single-detected-photon area distributions. The raw num-⁵⁸⁷
 532 ber of spikes is obtained in LUX by counting maxima in⁵⁸⁸
 533 the regions waveform which are above above the POD-⁵⁸⁹
 534 start threshold. A simple Monte Carlo model of spike⁵⁸⁹
 535 overlap in time, based on average S1 and single-photon⁵⁹⁰
 536 pulse shapes, was run to generate a look-up table of the⁵⁹¹
 537 most likely number of true photons as a function of raw⁵⁹²
 538 area and counted spikes. Tritium calibration S1s demon-⁵⁹³
 539 strated that the average of the simple area estimator for⁵⁹⁴
 540 bins of the combined estimator agree systematically to
 541 within 5% everywhere and to within 1% from 16 phd to⁵⁹⁵
 542 80 phd, above which point areas alone are used as pileup⁵⁹⁶
 543 becomes significant.⁵⁹⁷

544 The last step of event reconstruction is to account for⁵⁹⁸
 545 spatial and temporal variation in the detector response⁵⁹⁹
 546 and so calibrate raw pulse areas to quantities that are in⁶⁰⁰
 547 constant proportion to an event's light and charge wher-⁶⁰¹
 548 ever it occurred. The dominant sources of non-uniformity
 549 are the geometry-dependent probability for signal pho-⁶⁰²
 550 tons to be detected by the PMTs and, additionally for⁶⁰³
 551 S2, the time-varying concentration of impurities in the⁶⁰⁴
 552 xenon which capture ionized charge as it drifts towards⁶⁰⁵
 553 the liquid surface.⁶⁰⁶

554 Calibration maps of the relative response are obtained⁶⁰⁷
 555 by injecting a monoenergetic ^{83m}Kr source (see Sec-⁶⁰⁸
 556 tion V). They are used to derive, for all events with an⁶⁰⁹
 557 S1 and an S2 and hence a measured position, calibrated⁶¹⁰
 558 areas defined such that they would equal the raw pulse⁶¹¹
 559 area for events at the detector center were there to be no⁶¹²
 560 signal loss to impurities. The symbols $S1_c$ and $S2_c$ are⁶¹³
 561 used to denote these final, flat-fielded estimators of light⁶¹⁴
 562 and charge: S2 is always measured via pulse areas with⁶¹⁵
 563 $S1_c$ also using digital spike counts (or not) according to
 564 pulse size.⁶¹⁶

565 The absolute scales of scintillation photons and ioniza-⁶¹⁷
 566 tion electrons were obtained from a set of responses to⁶¹⁸
 567 monoenergetic ER sources using the Platzmann model⁶¹⁹
 568 (see section [sec:ER]); however, WIMP search does not
 569 rely on these scales as the detector's NR and ER re-⁶²⁰
 570 spondences in $S1_c$ and $S2_c$ are calibrated *in situ*.⁶²¹

571 The high-level output of the data processing frame-⁶²⁴
 572 work is thus a set of observables measuring position, light⁶²⁴
 573 and charge for each reconstructed event above threshold⁶²⁵
 574 in the active region of LUX: x , y , t_{drift} , $S1_c$ and $S2_c$.⁶²⁶
 575 The remainder of analysis consist of applying appropri-⁶²⁷
 576 ate event selection and making inference about physics⁶²⁸
 577 models by comparing observed and predicted distribu-⁶²⁹
 578 tions in these observables.⁶³⁰

IV. SIMULATIONS: LUXSIM – MATTHEW

A. Infrastructure: NEST + GEANT + data processing as for real data; Verifications - Last update 07-30-2015

The LUX simulation package, known as LUXSim [29], can be divided into 5 overarching, mostly serial functions:

- Recording of the energy deposited by different particles in different volumes at different times using Geant4 [30, 31]. Geant version 4.9.4 patch 4 was used.
- The production of both VUV scintillation photons and thermal ionization electrons which drift, using NEST: a different (though anti-correlated) number of each depending on the particle type interacting, the magnitude of LUX's drift electric field affecting energy partitioning, and energies of recoils [32, 33].
- Using the Geant4 optical model, photons from the initial primary scintillation in the liquid are propagated until reaching PMTs or becoming absorbed by impurities (simulated directly from within G4 by means of an exponential mean free path for photon propagation through the xenon) or by imperfectly reflective surfaces.
- Low-energy electrons liberated by an interaction are drifted up through the xenon using NEST, diffusing in three dimensions and being absorbed in a similar manner to the photons, but now using the empirically-determined (with Kr83m) electron absorption length. Once the electrons reach the gas, then NEST produces the secondary scintillation as a function of field, density, and gas region length. The electroluminescence photons are again simply propagated with G4 optical processes. (The drift and extraction fields are both sufficiently uniform in LUX that modeling them as scalar constants serves as an accurate representation for most purposes. See Section V C 3).
- QE's are simulated as a function of incoming photon wavelength, angle, temperature, and PMT variation. A full custom simulation for the unique DAQ takes numbers and arrival times of primary and secondary photons and generates output files from LUXSim that are in the identical format as empirical data and processed using the same data processing framework, enabling direct comparisons.

The component-centric approach provided by LUXSim makes it possible to define any parts of the detector, not just the PMT arrays, as sensitive volumes, ones where energy depositions and interactions along particle tracks are all recorded. This makes simulation testing and validation studies easier to perform. Although the NEST framework, based on earlier experiments' results,

is used for the absolute photon and electron yields, slight changes are made to the default approach and the values of various free parameters are fine-tuned in order to more precisely match LUX’s own calibration data at its particular electric field, for both ER and NR, as discussed in Section V next.

Full ER and NR simulations run through the data-processing chain are used to produce and vary the background and signal models respectively, for use in the PLR (Profile Likelihood Ratio, Section VI E). After vetting the simulation in terms of raw signal appearance as well as reproduction of calibration results, it can be used to produce ER and NR energy spectra that differ from those seen in the calibrations. The LUX background, overwhelmingly from ER, is considerably different in shape than the tritium beta spectrum, and different mass WIMPs produce distinct falling-exponential-like NR spectra. LUXSim was used to generate “pure” single-scatter event samples: for example, NR without ER contamination, misidentified multiple-scatter fiducial events, or multiple scatters with vertices outside the drift region (all these can occur especially with AmBe or ^{252}Cf sources). LUXSim combined with the Kr83m calibration of the position-dependent light collection is used to compensate for the fact none of the NR calibrations are uniformly distributed as a WIMP would be.

The LUX background model [34] is based on the measurements of the (trace) radioactive contamination of samples of many of the detector components from many separate counting experiments, the results of which were then input into the Monte Carlo. Simulated S1 and S2 spectra were compared with the actual background observed during the WIMP search run, in terms of not only the absolute count rate but also the position-dependent profile, crucial for the PLR (Figure ??). The primary background constituents are ERs from the PMTs’ uranium- and thorium-chain gamma-rays. In order to match the data most precisely, the initial contamination values required fine-tuning within errors.

The simulated single PE area (in voltage) and shape (roughly Gaussian) were matched by finding single PEs in LED calibration and general background data. The size of SEs in terms of number of PE could be predicted from first principles by calculating the absolute S2 photon yield [35, 36] and knowing the light collection efficiency for the gas region from optical simulations, and the measured QE. This method agrees within 10% of the observed SE pulse area [37, 38]. The width and general shape are matched using a Gaussian distribution for the absolute yield in the gas gap and binomial light collection and QE, yielding a slightly non-Gaussian shape that is indeed observed in data. For comparisons of both the single PE and SE between sim and data, see Figures 18 and 19 in Section V. The SE width in PE number is about twice what one would expect from a Poisson process (\sqrt{N}), though this can easily be explained as due to field non-uniformities between the anode and liquid-gas border [39]. The temporal profile of an SE or an S2 of

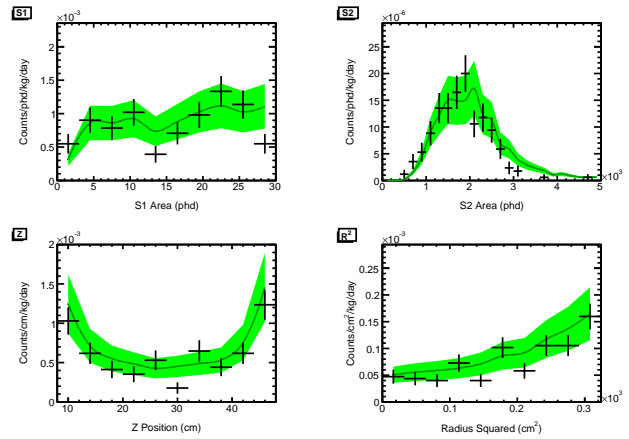


FIG. 12. The absolute number of background events as a function of the S1 size, and as a function of the S2 size, as well as the profile of the number of events as a function of depth and radius, combining all known sources of background. The S1 is cut off at 30 phd here, causing the peak in the S2 spectrum.

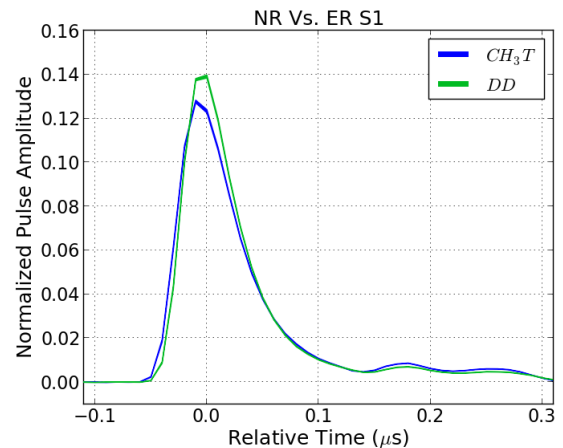


FIG. 13. **PLACEHOLDER** Comparison of S1 profile in time for ER (tritium) and NR (DD) events between simulation and data. SIM COMING.

any size in general was predictable based on the known electron diffusion constants in liquid xenon, the electron drift speeds in liquid and gas, the electron extraction delay at the liquid surface, the (small) light travel time to the PMTs, and the singlet and triplet time constants characteristic of the excited molecular (excimer) states of xenon dimers; the last two points, plus the time it takes for ionization electrons to recombine with ions, allow reproduction of the S1 pulse shape as well [40]. See Figures 13 and 14.

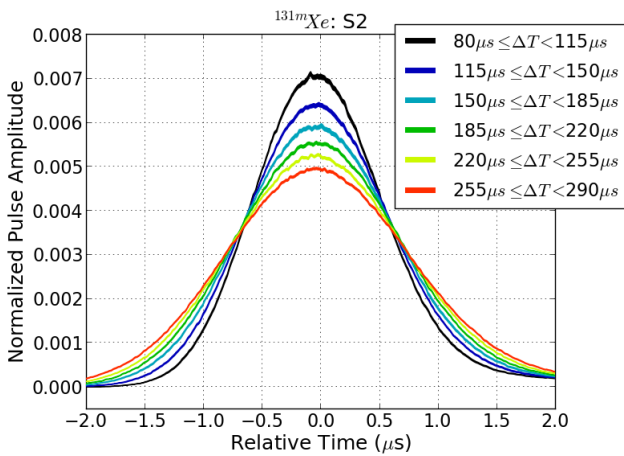


FIG. 14. **PLACEHOLDER** Comparison of S2 profile in time for Xe-131m ER (164 keV) events between simulation and data. SIM COMING.

B. Optical model - Last update 07-30-2015

Unlike NEST, the model for photon propagation is detector-specific. The free parameters varied within the Geant4 model were

- the reflectivity of the stainless steel field-generating grids and of the PTFE in liquid and gas separately
- the exponential photon mean free path separately for liquid and for gas
- an overall QE re-normalization to account for a ~10% increase at cryogenic temperatures [41, 42]
- the reflectivity of the aluminum flashing on the PMT quartz faces

The indices of refraction of xenon and quartz were based on previous data [43, 44] while the Rayleigh scattering length came from a theoretical calculation [45]. This list was further narrowed down to the major factors with the most impact, namely the reflectivity of the PTFE walls in the liquid and the photon absorption length in liquid. Since for both an increase implies better light collection, they are partially degenerate, but not entirely so due to the ability to compare S1, S2, the position dependence of each, and the ratio of light in the top or bottom PMTs to the total light collected (Figures 15, 16, and 17). The most sensitive means by which to create the best-fit optical model was the S1 pulse area as a function of depth from mono-energetic peaks in the high-statistics ^{83m}Kr calibration data. The radial dependency was secondary, due to the symmetry of the detector, broken versus depth due to the presence of the border between gas and liquid near the top of the TPC (leading to total internal reflection).

After the relative light collection efficiency as a function of depth and radius was matched for the S1 with LUXSim, it was cross-checked by looking at the SE signal size and the position dependence of the S2. (Using ^{83m}Kr leads to a model valid for all particles because, once light is generated, the nature of the original incident particle is irrelevant, in terms of photon fate.) Then the absolute photon detection efficiency, a combination of light collection and QE, for the center of the detector was simulated in order to ground the relative-only efficiency comparison. The resulting S1 photon detection efficiency (or, g_1 as defined later in V D) of $11.7 \pm 0.3\%$ is in excellent agreement with the $11.7 \pm 0.3\%$ determined in Figure 37. This is consistent with our previously reported result [19] also based on simulation of $14 \pm 1\%$, after accounting for the discovery of a $\sim 20\%$ chance for the R8778 PMTs to generate 2 PE per 1 actual detected photon [16, 46], implying the 14% was actually $14/1.2$ from the beginning (and with the “Doke plot” method resulting in a reduction in error from 1 to 0.3% compared to earlier approaches, Figure 37 in Section V D). Lastly, comparison of mono-energetic S1 peak mean positions to NEST predictions agrees within known uncertainties as well (Figure ??). Our revised calculation of the extraction efficiency (of 42% versus the previous 65%) is now in better agreement with [47] and [48] versus [49], especially after accounting for our liquid level being lower than nominal based on a deeper look at level sensor data, thus leading to a lower extraction electric field than originally estimated.

However, Figure 15 demonstrates a physics-motivated approach based on tuning detector material optical properties like reflectivity is still imprecise. It cannot for instance account for all potential microscopic surface deformations creating position-dependent reflectances on the same surface, or exotic, non-exponential mean free paths for photon absorption by impurities in xenon. Thus, in order to ensure the most precise possible background and signal models for the sensitivity calculation, the position corrections based on the ^{83m}Kr calibrations (see Sections III D 4 and V and the data within Figure 15) applied to the real data sets were also used to generate empirical S1 and S2 3D hit map look-up libraries for every PMT. These libraries avoided the need for photon propagation in every single full Geant simulation, and thus increased run time by two to three orders of magnitude while looking more like data.

LUXSim has achieved an unprecedented degree of agreement between Monte Carlo simulations and empirical results across many dimensions, including S1 and S2 yields, energy resolution, and pulse shapes.

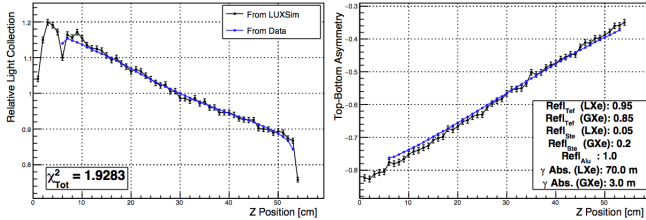


FIG. 15. PLACEHOLDER S1 fits. χ^2 is calculated for both the relative light collection efficiency at the left and the top-bottom asymmetry at right, where the latter is $(T-B)/(T+B)$, where T and B are the amount of S1 light recorded in the top and bottom PMT arrays respectively (simultaneous fit to both quantities).

quantity	region	value	error
PTFE reflectivity	liquid	0.95	
PTFE reflectivity	gas	0.85	
stainless reflectivity	liquid	0.05	
stainless reflectivity	gas	0.20	
Al reflectivity	n/a	1.00	
photon absorption	liquid	70m	
photon absorption	gas	3.0m	

TABLE I. Best fit optical parameters from the figure at top.

V. CALIBRATIONS

A. Response to single quanta: SPE size, SE size and corrections for x,y,z – Aaron - Last update 06-15-2015

Because both the scintillation and the ionization signals are detected by the photomultiplier tubes (PMTs), a basic unit of measurement in LUX is the photoelectron

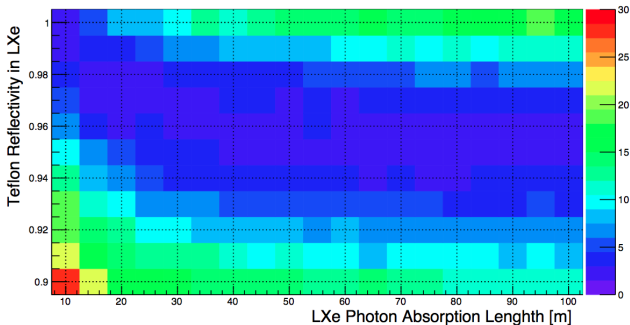


FIG. 16. PLACEHOLDER χ^2 map for Teflon reflectivity and photon absorption length in liquid xenon, the two free parameters which have the biggest impact on both relative and absolute light collection. One can see the degeneracy between the reflectivity of the Teflon and the absorption length for photons in the liquid, which each have similar effects on the reduction in the light collected. As the former asymptotes to $\sim 95\%$, a reasonable value [50], the latter approaches infinity.

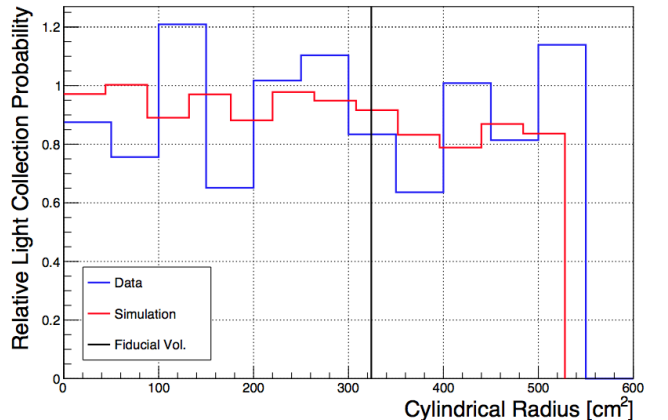


FIG. 17. PLACEHOLDER Demonstration of good agreement on the S2 profile versus radius between calibration data and simulation, relative to the detector center.

(phe). In order to stimulate the emission of single phe for calibration purposes, six blue light-emitting diodes (LEDs), located in the LXe but outside of the TPC, are individually pulsed at a rate of 1 kHz and a pulse width of 100 ns. The pulse amplitude is set so that a given PMT sees no signal for most LED pulses, in which case the number of phe observed per LED pulse that PMT is Poisson distributed. If the amplitude is small enough, LED pulses that show non-zero signal will be a nearly pure sample of single phe, and can be used to extract the average amplification (i.e. the ‘gain’) of the PMT.

The single-phe response of one LUX PMT is shown in Figure 18 (gray histogram) as an example. The gain of the PMT, defined as the average number of electrons collected at the anode given a single electron emitted from the photocathode, is on average YY, with a resolution (σ/μ) of 35%. LED calibrations are carried out weekly throughout the duration of the experiment.

The method of ionization readout used by the LUX experiment is sensitive to single electrons. Electrons emitted from an interaction site travel through the liquid under the influence of the applied drift field until they reach the liquid surface. The liquid level is located between the gate and anode grid electrodes, and is therefore influenced by a different electric field than what is applied to the bulk of the liquid. This electric field is known as the extraction field, and is used to transport the drifting electrons from the liquid to the gas. Once in the gas, the electrons collide with gaseous xenon atoms and induce secondary scintillation light as they travel to the anode. A fraction of these secondary photons are detected by the PMTs, and their intensity is proportional to the ionization signal.

Typically in the use of PMTs, a single phe is synonymous with a single detected photon. However, the LUX experiment has discovered that the detection of a single VUV scintillation photon often causes the emission of two phe. Because the quantum efficiency (QE) reported by

the PMT manufacturer is defined as the number of phe₈₅₉ emitted from the photocathode per incident photon, this₈₆₀ effect leads to a difference between the QE and the pho-₈₆₁ ton detection efficiency, a fact that has important impli-₈₆₂ cations when trying to reconstruct the energy of an event₈₆₃ based on absolute yields [46].

The rate of double-phe emission-per-VUV-photon is₈₆₅ measured in two ways, one using scintillation photons₈₆₆ emitted by the liquid, and another using scintillation₈₆₇ photons emitted by the gas. For the former, a sample₈₆₈ of events from a CH₃T calibration are selected for which₈₆₉ the total S1 light collected for each event is on average₈₇₀ ~ 5 phe. With this selection, the average number of phe₈₇₁ collected in a given PMT is less than 0.05 per event. The₈₇₂ number of detected photons—not the number of phe—is₈₇₃ Poisson distributed in this PMT (similar to the strategy₈₇₄ utilized in LED calibrations). If μ is the average num-₈₇₅ ber of detected photons per event for a given PMT, the₈₇₆ fraction of non-zero events which are contaminated by₈₇₇ multiple detected photons is $1 - (\mu e^{-\mu}) / (1 - e^{-\mu})$. There-₈₇₈ fore, taking $\mu < 0.05$, the set of non-zero hits (for that₈₇₉ PMT) is a nearly pure sample of single detected pho-₈₈₀ tons, with multiple detected photons contributing less₈₈₁ than 2.5%. Figure 18 shows, for an example PMT, a₈₈₂ comparison between the spectrum obtained from the (op-₈₈₃ tical) LED calibration and the (VUV) CH₃T calibration₈₈₄ (“VUV (liquid”)). The shoulder on the tail of the single-₈₈₅ phe peak is readily visible, which indicates the presence₈₈₆ of this double-phe emission process. Plots such as this are₈₈₇ used to construct a “VUV gain” for each PMT, which in-₈₈₈ dicates the average number of electrons collected at the₈₈₉ PMT anode for a single detected VUV photon. In this₈₉₀

case the basic unit of measurement is no longer the number of phe, but the number of detected photons (dph).

The second method for measuring VUV-photon re-₈₉₁ sponse uses electroluminescence light from the gas region,₈₉₂ in the form of single-electron (SE) ionization pulses from₈₉₃ calibration data. Photoionization of impurities in the₈₉₄ bulk liquid following ^{83m}Kr S1s provide a large and and₈₉₅ pure sample of SEs. Light from each extracted elec-₈₉₆ tron is approximately uniform in time over the 1 μ s drift₈₉₇ from liquid surface to anode, and sums to an average₈₉₈ of 25 detected photons across the 122-PMT array; the₈₉₉ signal therefore appears in individual PMT traces pre-₉₀₀ dominantly as single photons or two clearly separable₉₀₁ photons (single photons having FWHM around 30 ns).₉₀₂ The mean area of the single photon response in a given₉₀₃ PMT is obtained in three steps. First, the mean area of₉₀₄ those SE responses with one identified maximum above₉₀₅ a 1.4 mV threshold is calculated. Second, the number of₉₀₆ unresolved pileup events contributing to that mean is es-₉₀₇ timated from those responses with two photons resolved₉₀₈ in time: the interval between first and last DAQ sam-₉₀₉ ples above threshold for the two-spike responses has the₉₁₀ expected linear distribution above 7 samples, which is ex-₉₁₁ trapolated and integrated over the region of smaller inter-₉₁₂ vals, where the two photons may not be resolved. Third,₉₁₃ the mean area of single spike events is corrected for the₉₁₄ pileup, with the area of the contaminating 2-photon₉₁₅ responses taken to be the same as the resolved 2-photon₉₁₆ responses. This correction is small, on average 3% for₉₁₇ top array PMTs and 1% for bottom array PMTs. The₉₁₈ resulting gain estimates are systematically 2.5% higher₉₁₉ than the liquid-scintillation estimates, which may be due₉₂₀ to the difference in scintillation wavelength. The liquid-₉₂₁ scintillation values are adopted since it is for S1 light that₉₂₂ the number of detected photons implies a detection effi-₉₂₃ ciency for the fundamental signal quanta (for the case of₉₂₄ ionization, any pulse-area unit used for both S2s and SEs₉₂₅ cancels out when one divides to estimate electrons).

The ionization signals collected by the LUX detector are intrinsically measured as a pulse of VUV pho-₉₂₆ tons. The size of these pulses can be understood more₉₂₇ usefully by reporting the absolute number of electrons₉₂₈ creating the signal. Doing so requires a calibration of₉₂₉ the detector to single electrons. Fortunately, single elec-₉₃₀ trons can be seen being periodically emitted from the₉₃₁ liquid surface, a phenomenon which has been described₉₃₂ in the ZEPLIN-II [51], ZEPLIN-III [52], XENON10 [53],₉₃₃ and XENON100 [54] experiments. A sample of pure sin-₉₃₄ gle electrons is selected by searching the event record in₉₃₅ ^{83m}Kr events between the S1 and S2 signals. Since it is₉₃₆ known that these events are essentially single-site, any S2₉₃₇ features in the event record between S1 and S2 are un-₉₃₈ likely to be anything besides single electrons. The rate of₉₃₉ single electrons is low enough that the probability for two₉₄₀ electrons to randomly overlap in time is negligible. Figure₉₄₁ 19 shows the spectrum of the ionization signal from₉₄₂ single electrons, in units of number of detected photons.₉₄₃ As the proportional scintillation process depends on the₉₄₄

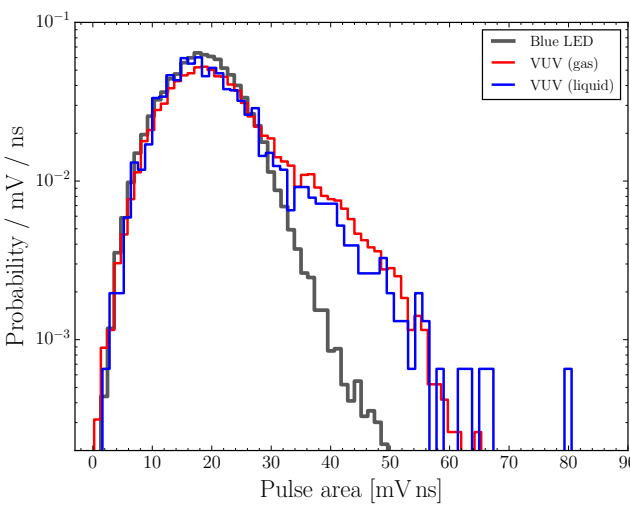


FIG. 18. The pulse-area spectrum from single photoelec-₉₁₁ trons (“blue LED”), single-detected VUV photons emitted₉₁₂ from gaseous xenon [“VUV (gas)”] and liquid xenon [“VUV₉₁₃
914 (liquid)”). The shoulder apparent in the spectra from single-₉₁₅
emission process.

extraction field and gas gap [?], variations of these parameters across the plane of the liquid surface can lead to variations of the average single-electron size. Figure 20 shows the average of the single-electron distribution in this plane; we note that the $1-\sigma$ variation in the mean in this plane is $XX\%$, while the $1-\sigma$ statistical variation at a single position is $YY\%$. Figure CC shows the variation in the average single-electron size over the duration of the science run.

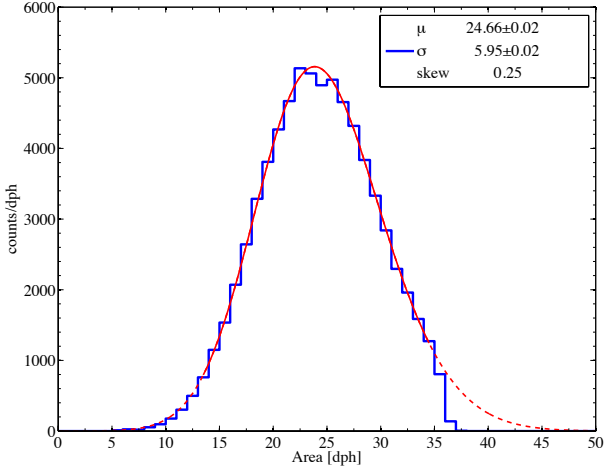


FIG. 19. Spectrum of ionization signals from single electrons. The spectrum is fit with a skew-normal distribution, giving a mean of 24.66 ± 0.02 (stat) dph and a $1-\sigma$ of 5.95 ± 0.02 (stat) dph.

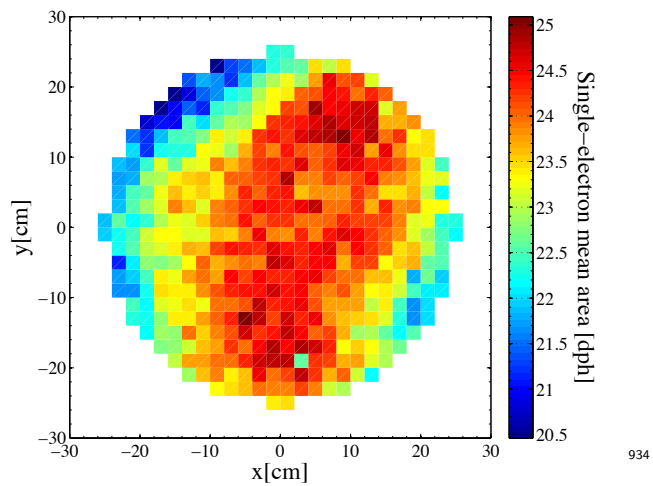


FIG. 20. Variation of the mean of the single-electron distribution in the plane of the liquid surface.

B. Stability: – Carlos/Aaron

1. PMT Gain Stability - Last update 06-15-2015

The LED calibrations, described above, are measured periodically over the course of the WIMP search. An example of ten PMT gains are shown in Figure 21. For all PMTs, the relative level of fluctuations are shown in Figure 22; most gains are stable to better than 2% (std/mean).

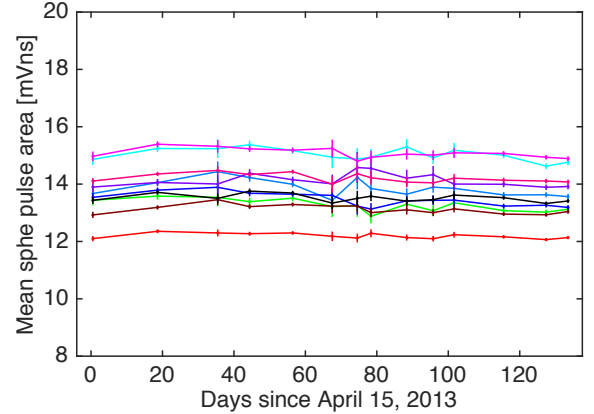


FIG. 21. Gain time trend, Example of 10 PMTs

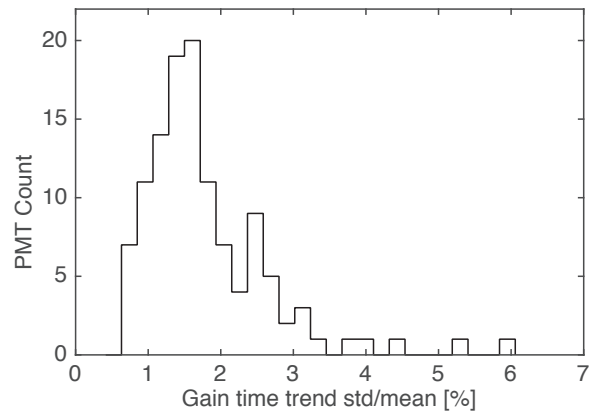


FIG. 22. Distribution of Gain Time Trend Variation

2. SE Size Stability - Last update 06-15-2015

The S2 gas gain is determined by a number of factors, including the pressure of the gas, the level of the liquid, and the extraction electric field. All these parameters are of course monitored by the slow-control system, but the important information is their combined effect on the

gas gain. Using ^{83m}Kr calibration data, the average size of a single-electron S2 is computed periodically over the course of the WIMP search, shown in Figure 23. These data indicate that the single-electron size is stable at the level of 1.4% in this time range.

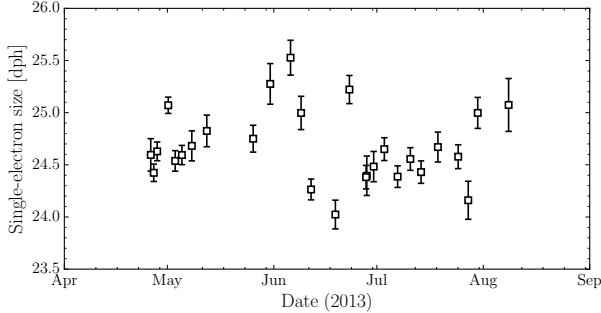


FIG. 23. The variation in the size of a single-electron S2 pulse over the course of the WIMP search.

945 3. - Last update 06-15-2015

946 Residual O₂ impurities can capture electrons as they
947 drift through the liquid, thus producing a depth-
948 dependent attenuation of the ionization signal. The con-
949 centration of O₂ can be expressed as the average time
950 that an electron will propagate before capture; this quan-
951 tity is known as the electron lifetime. As this quantity
952 varies over the course of the experiment (and is used to
953 correct observed ionization signals), it is measured peri-
954 odically during the WIMP search. Periodic calibrations
955 with ^{83m}Kr , in a technique similar to those described in
956 [55, 56], are carried. This source decays via the emission
957 of 32.1 keV followed by 9.4 keV; the half-life of the 9.4 keV
958 state is 154 ns. This short half-life means that they oc-
959 cur essentially at the same location in space, and also
960 that they often occur too close in time to be resolved
961 as separate pulses. The depth-dependence of the com-
962 bined 41.5 keV ionization signal is measured, from which
963 the electron lifetime is calculated. Figure 24 shows the
964 measured electron lifetime during the WIMP search.

965 4. Kr-83 Light Yield Stability - Last update 06-15-2015

966 The stability of the ionization and scintillation re-
967 sponse of the LUX detector is monitored with the pe-
968 riodic ^{83m}Kr calibrations. Because this decay always re-
969 leases the same energy, the variation of the scintillation
970 and ionization signal from ^{83m}Kr over time provides a di-
971 rect handle on the stability of the detector response. Fig-
972 ure 25 shows these responses over the time period of the
973 WIMP search. The relative time variation (stdv/mean)
974 of the scintillation response from these calibrations is
975 0.6%, while that of the ionization signal is 2.4%.

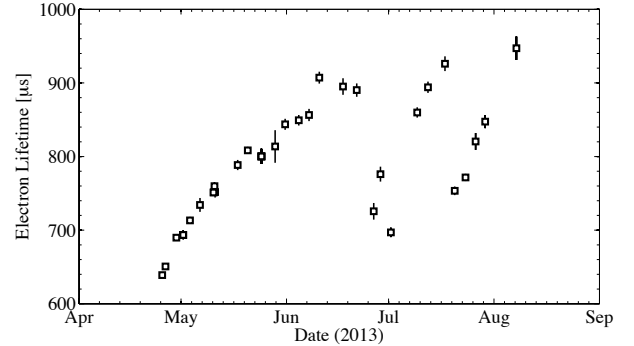


FIG. 24. Electron lifetime over time.

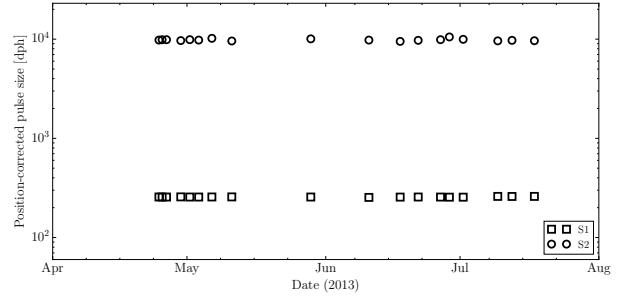


FIG. 25. The scintillation (squares) and ionization (circles) response of the LUX detector over time to the decays of ^{83m}Kr .

C. Position Reconstruction – Kevin/Carmen

1. Measuring the fiducial volume - Carmen - Last update 08-11-2015

The total xenon mass in the active volume between the cathode and the gate grids is determined as:

$$M_{\text{Xenon}} = 3R^2 L \frac{\rho_{\text{Xenon}}}{1000} = 250.9 \pm 2.1 \text{ kg} \quad (1)$$

where R=24.48±0.05 cm corresponds to the distance between the center of the detector and corners of the PTFE panels; L = 48.32 ± 0.34 cm is the distance between the cathode and the gate; and ρ=2.887±0.005 g/mL is the xenon density at 173.19±0.07 K.

The fiducial region is defined as a cylindrical volume that select events with radius less than 20 cm and a drift time between 38 and 305 μs . To calculate the xenon mass in this volume, we need to convert the drift time to z position, measured relative to the surface of the PMTs in the bottom array. The conversion is given by:

$$z = s_c + L - v_d (\tau - \tau_g) \quad \text{with} \quad v_d = \frac{L}{(\tau_c - \tau_g)} \quad (2)$$

where v_d is the drift velocity, measured at 0.1518±0.0011 cm/ μs (see Fig. 26); s_c = 5.6 cm is the distance between

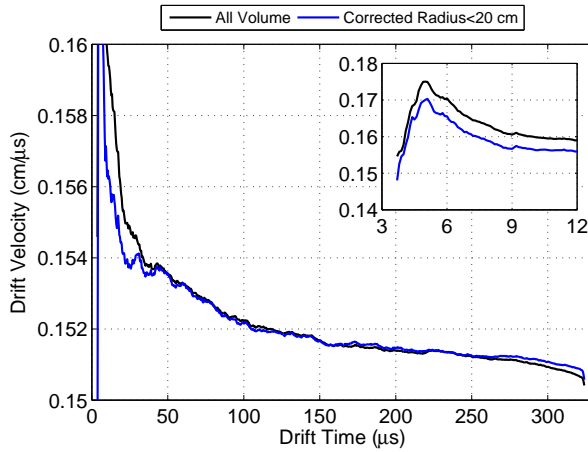


FIG. 26. Drift velocity versus drift time.

cathode and the surface of the PMTs; and τ_g and τ_c correspond to the drift time of events at the gate and at the cathode, respectively. These values are estimated using the krypton calibration data, from which we obtain $\tau_g = 3.4 \pm 0.4 \mu\text{s}$ and $\tau_c = 322.3 \pm 0.4 \mu\text{s}$. Using these values, we calculate a fiducial volume mass of $147 \pm 1 \text{ kg}$.

The fiducial mass of the detector can also be calculated using the distribution of the tritium events in the detector. This method takes the ratio of the observed number of tritium events in the fiducial volume to the number of events between the cathode and the gate, and then multiplies it by the total xenon mass between the cathode and the gate. This method has the advantage of not needing the dimensions of the the fiducial volume, such that the effects of any possible systematic uncertainty from the drift time conversion and position reconstruction are eliminated.

For this calculation, the tritium events are selected using the same quality cuts applied in the WIMP search data (described in section VI A). Additionally, the events from the first hour after the tritium injection are not included to ensure uniform distribution of tritium events in the detector. The mixing time observed for $83mKr$ injections was observed to be less than 10 minutes, and a similar mixing time is expected for tritium injections. After the mixing period, the distribution of tritium events is very uniform along the radius, with only a small accumulation of events near the walls of the detector, as shown in figure 27.

Using a drift time cut between $3.4 \mu\text{s}$ and $327 \mu\text{s}$ to select events in the active volume between the cathode and the gate grid, we observe $(223.1 \pm 0.5) \times 10^3$ tritium events. A fiducial volume cut selects events with a drift time between $38 \mu\text{s}$ and $305 \mu\text{s}$ and a radius smaller than r . The ratio between these two event counts is multiplied by the xenon mass between the gate and cathode, calculated in Eq. 1. Fig. 28 shows the fiducial mass as

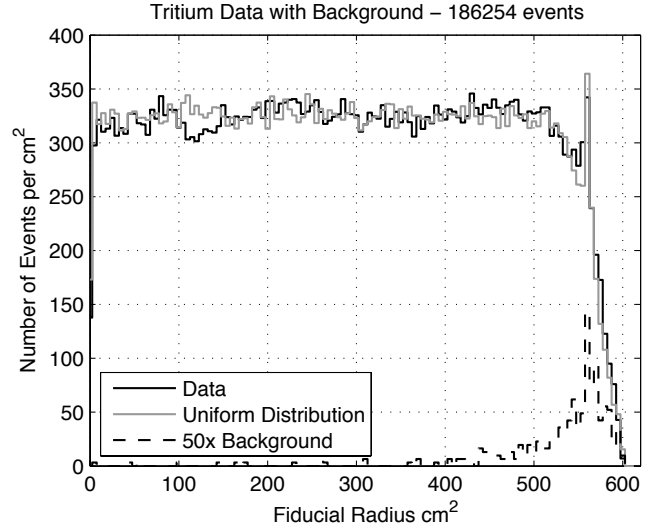


FIG. 27. Histogram of the number of the observed tritium events as function of the corrected radius and for a drift time between $38 \mu\text{s}$ and $305 \mu\text{s}$ (solid black line). The gray line represents a perfectly uniform distribution of events. The dotted line represents an estimate of the background observed during the lifetime of the tritium calibration multiplied by a factor of 50.

function of the radius r . For a radius of $r = 20 \text{ cm}$, the number of events observed is $(129.1 \pm 0.4) \times 10^3$, which yields a fiducial mass of $145 \pm 1 \text{ kg}$.

Fig. 29 shows the difference between the mass calculated using the event counting method, and the mass calculated directly from the geometry, as function of the fiducial volume radius. The difference between these two methods is smaller than 1.4 kg for any fiducial radius.

2. XY Position Uncertainty - Kevin - Last update 06-15-2015

The statistical uncertainty on XY position reconstruction is most naturally handled in polar coordinates. In this case the uncertainty breaks down into three categories:

1. The centripetal uncertainty: the radial uncertainty in the direction towards zero radius
2. The centrifugal uncertainty: the radial uncertainty in the direction towards the wall
3. The polar uncertainty: the uncertainty in the polar angle, treated as symmetric

This parameterization is convenient as the radial position is paramount toward whether an event looks more signal-like (towards the center of the detector) or background like (toward the wall of the detector). These three uncertainties are calculated from the Mercury error oval

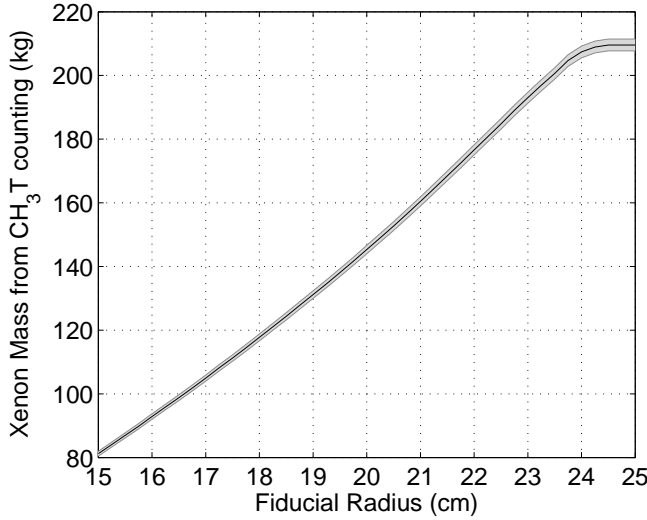


FIG. 28. Xenon mass calculated directly from tritium counting as function of the radius of the fiducial volume. The 1 sigma band is represented by grey band. The drift time considered is between $38 \mu\text{s}$ and $305 \mu\text{s}$ and the mass between the gate and anode is $250.9 \pm 2.1, \text{kg}$.

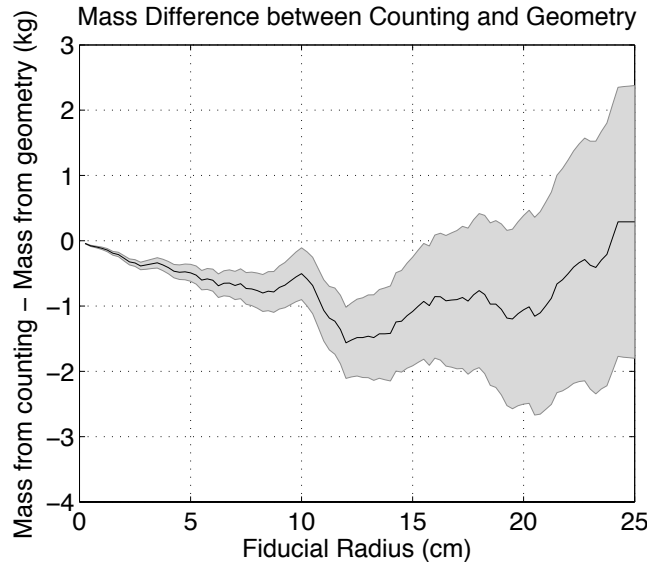


FIG. 29. Difference between the xenon mass calculated from the counting of tritium events and the xenon mass obtained from the geometry of the fiducial volume as function of the radius of the fiducial volume.

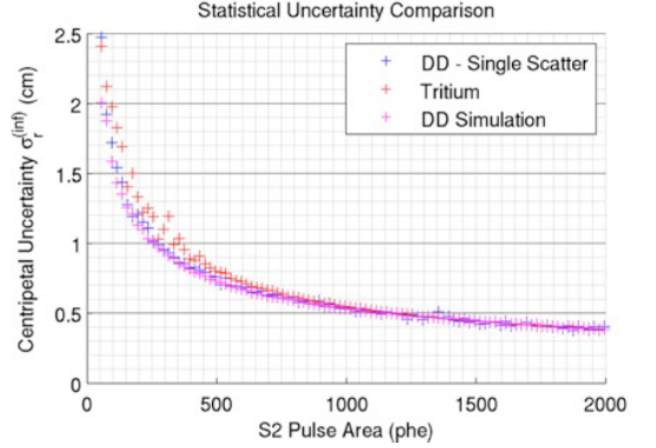


FIG. 30. **PLACEHOLDER** Comparison of centripetal uncertainties in Mercury in DD data (blue crosses), tritium data (red crosses), and DD simulation (magenta crosses). The three agree for S2 size above 500 phd. Below 500 phd the tritium uncertainties come out slightly larger.

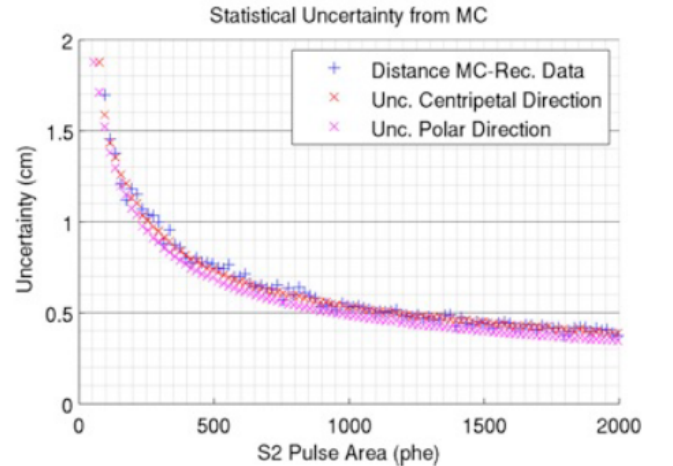


FIG. 31. **PLACEHOLDER** Comparison of the centripetal and polar uncertainties in DD simulations to the RMS of the difference between the reconstructed position and the true position.

uncertainties with minor disagreement below 500 phd.

The advantage of comparing the uncertainty in data to a simulation is that in a simulation the true event locations are known, allowing for a consistency check as shown in figure 31. The calculated statistical uncertainties are very close to the differences between the real and reconstructed positions.

In addition to the statistical uncertainty on the XY ($R\theta$) positions there is a systematic uncertainty which can be calculated using the position of events in the beam from DD calibrations. Because the DD is collimated beam, the events in the DD calibrations will appear in a line in the XY ($R\theta$) plane. The deviation from a straight

1058 based on the χ^2 fit. Figure 30 shows the centripetal
 1059 uncertainty versus S2 size for DD data, tritium data,
 1060 and DD simulations. Here the uncertainties, binned by
 1061 S2 size, are the average over the entire fiducial volume.
 1062 Unsurprisingly the uncertainty decreases as S2 size in
 1063 creases, as a result of there being more information car-
 1064 riers. For large S2s, above 500 phd, the three have simila-
 1065
 1066
 1067
 1068
 1069
 1070

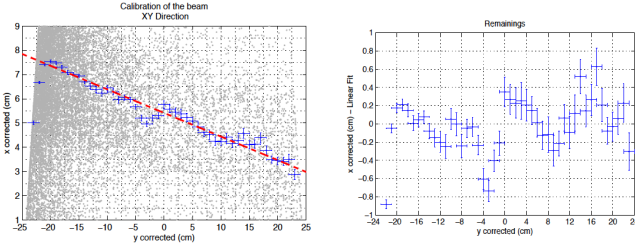


FIG. 32. **PLACEHOLDER** *Left:* The blue crosses show the average reconstructed X position as a function of reconstructed Y from DD calibration data. In both cases X and Y are corrected for the effects of the non-uniform field electric field. The dashed red line shows a linear fit to the DD beam direction *Right:* Deviation from the linear fit in the X direction.

line can therefore be used as a measure of the systematic uncertainty in the positions reconstruction. A linear fit to the DD path and the reconstructed XY position in the DD data are shown in 32. The maximum deviation from the linear fit within the fiducial volume is 7 mm.

3. Effects of non-uniform field - Kevin - Last update 06-15-2015

Due to field leakage through the cathode, the electric field in the active xenon is not perfectly uniform, having a small radial component. Figure 33 shows the reconstructed positions of events from ^{83m}Kr calibrations. The non-axial component to the field results in the electron cloud from an event being pushed inward, away from the wall of the detector. Because the position reconstruction is performed using the S2 signal, the scatters will be assigned an XY position based on where in the liquid the electrons are extracted. Therefore the electron cloud is pushed towards the detector center and the reconstructed XY-position will be different from the true XY-position.

In order to understand this phenomenon the detector electric field was modeled in two dimensions using COMSOL version 4.3b. The model was assumed to be axisymmetric and included the grids and insulators with their proper voltages and dimensions. The predicted field strength is shown in figure 34. At high radius the field lines become non-parallel, leading to events being reconstructed at smaller radius than the true event position. Along the vertical axis of the detector ($X=Y=0$) the field varies from 120 V/cm just above the cathode to 220 V/cm just below the gate. This variation has a negligible affect on the light and/or charge yields from low-energy nuclear or electron recoils.

Because the ^{83m}Kr is distributed uniformly throughout the detector, it can be used to produce a mapping of reconstructed XY positions to real XY positions. The detector is cut into 30 μs slices in drift time. For each slice in drift time, the detector is segmented into 60 sections in

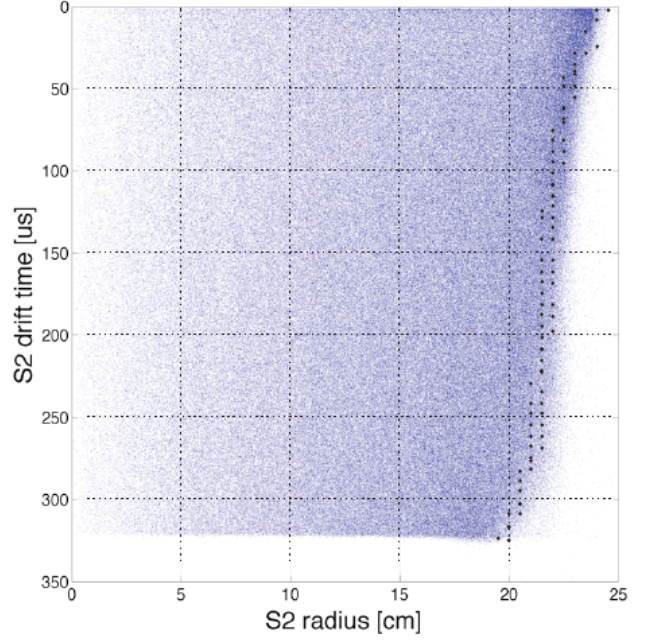


FIG. 33. **PLACEHOLDER** Reconstructed squared radius versus drift time for events from ^{83m}Kr calibrations. The non-radial component to the electric field pushes electron produced by ionizing radiation closer to the middle of the detector as they drift to the top. The black dots indicate the expected reconstructed edge of the detector volume as predicted by the electric field model.

the polar direction. The first 30 minutes of any injection are ignored to ensure enough time for uniform mixing. The remaining events in each section are placed into 600 uniform radial bins and the average radius in each bin is used to calculate the radial correction. This scheme enforces that the reconstructed positions be radially uniform within each drift time slice. Figure 35 shows the effects of this radial correction. Effects of non-uniform fields on drift time are negligible.

D. Electron-recoil response – Carter - Last update 07-03-2015

a. Combined energy model for electron recoils We interpret single-scatter events in the TPC with the combined energy model[57]:

$$E_{total} = W \cdot (n_e + n_\gamma) = W \cdot \left(\frac{S1}{g_1} + \frac{S2}{g_2} \right) \quad (3)$$

where g_1 and g_2 represent gain factors that convert S1 and S2 signals to electron number (n_e) and photon number (n_γ). W is the energy scale factor of LXe in units of eV/quantum. g_1 is the product of the average photon collection efficiency and the average QE of the PMTs, while

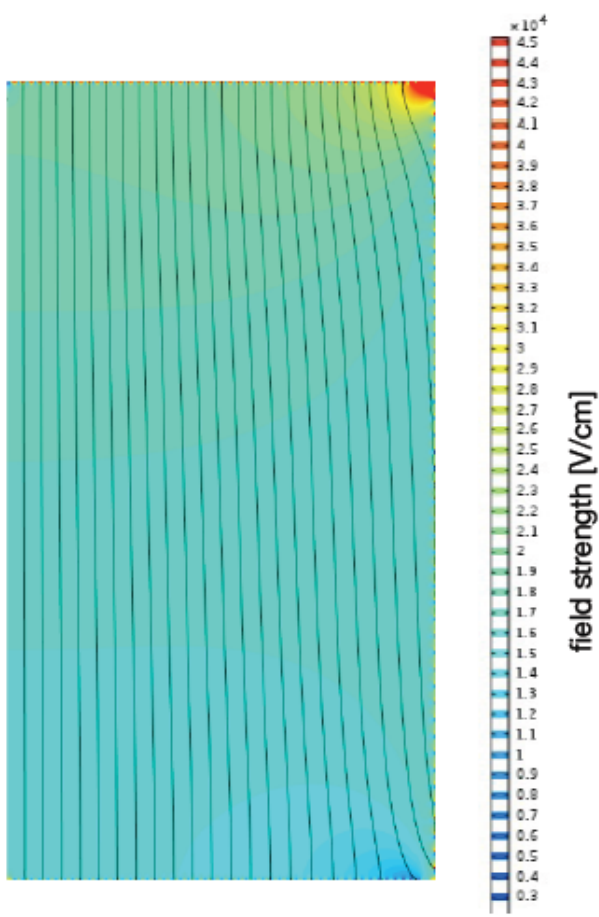


FIG. 34. **PLACEHOLDER** A two dimensional electric field model of the drift field in LUX performed using COMSOL 4.3b. At high radius the electric field lines are no longer parallel, leading to electrons drifting toward the center of the detector.

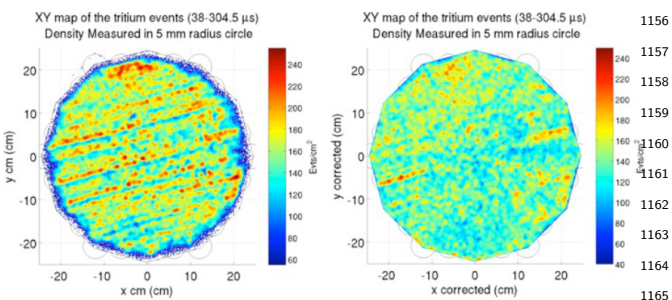


FIG. 35. **PLACEHOLDER** Right: uncorrected XY positions for ^{83m}Kr data. Left: corrected XY positions for the same ^{83}Kr data

Source	E (keV)	Type	Origin
^{127}Xe	5.3	L shell x-ray	Run 3 Data
^{83m}Kr	41.55	IC	internal calibration source
^{131}Xe	163.9	IC	early Run 3 Data
^{127}Xe	208.3	γ	Run 3 Data
^{129}Xe	236.1	IC	early Run 3 Data
^{127}Xe	409	γ	Run 3 Data
^{214}Bi	609	γ	detector background
^{137}Cs	661.6	γ	external calibration source

TABLE II. Table of sources used in the Doke plot analysis of Fig. 37. All source data are collected at 180 V/cm. The energy of both ^{127}Xe lines includes gammas and x-ray emission. IC = internal conversion.

1135 g_2 is the product of the electron extraction efficiency at
1136 the liquid-gas surface (ϵ_{ee}) and the single electron size
1137 (SE). For ER events in LUX we assume a constant W
1138 value of 13.7 eV/quantum[58].

1139 The gain factors g_1 and g_2 may be determined by ob-
1140 serving two or more ER line sources of known energy in
1141 which the average light and charge yields differ. g_1 and
1142 g_2 are then fixed by requiring that E_{total} computed with
1143 Eq. 3 reproduces the true energy of each source. In ER
1144 events the average yields vary with energy and electric
1145 field due to changes in the average recombination of ion-
1146 ization electrons with Xe^+ ions.

We use the eight sources listed in Table II to extract values for g_1 and g_2 in LUX. A scatter plot of S1 vs S2 for this data is shown in Fig. 36. A strong anti-correlation between S1 and S2 is apparent in each line due to recombination fluctuations. We fit a rotated two-dimensional gaussian to determine $\langle S1 \rangle$ and $\langle S2 \rangle$ for each line source. To reduce the dependence of the result on the data selection we iterate each fit by selecting data within two gaussian widths of the mean as determined by the initial fit. Variation in the S2 signal and S1 signal due to PMT saturation and single electron size variation are included as systematic errors in each fit.

*** Update the Doke Plot, and the Density plot to match the same source We extract g_1 and g_2 by plotting $x = \langle S2 \rangle / E$ vs $y = \langle S1 \rangle / E$ for each source and electric field value as shown in Fig. 37. We perform a linear fit $y = mx + b$ to the eight points, where $m = -g_1/g_2$, and $b = g_1/W$. We find $g_1 = 0.117 \pm 0.003$ and $g_2 = 12.1 \pm 0.8$, implying $\epsilon_{ee} = 0.491 \pm 3.2$. The errors are determined by toy Monte Carlo where each of the eight points is varied within its error. The extracted value for g_1 is in good agreement with the results of the optical model described in section IV B.

The observed value of ϵ_{ee} can be compared to previous measurements if the electric field value above and

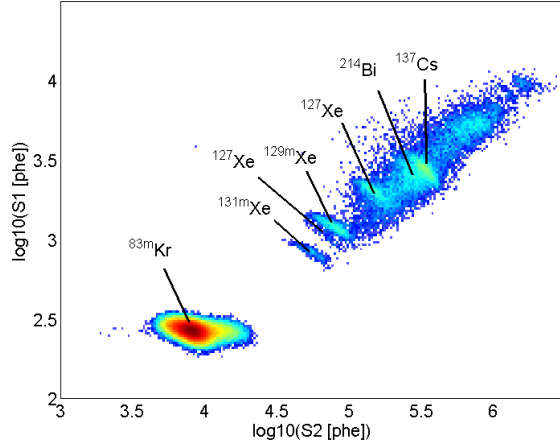


FIG. 36. S1 vs S2 for a compilation of LUX line source data. ^{83m}Kr and ^{137}Cs data are collected during dedicated calibration runs. All other lines are present in the low background WIMP search data. ^{129}Xe and ^{131}Xe are only present early in Run 3 due to their cosmogenic origin. The anti-correlation between S1 and S2 is due to recombination.

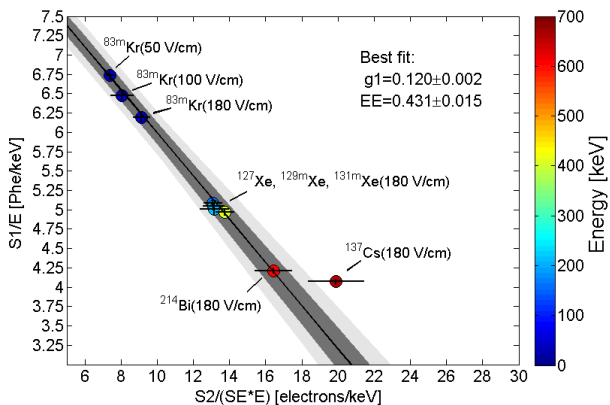


FIG. 37. Extraction of gain factor g_1 and g_2 according to the method described in the text. Each point represents a single line source listed in Table II.

results are consistent with g_1 and g_2 measured from the seven monoenergetic peaks within one sigma. [59].

E. Electron-recoil model

The electron recoil model is based upon the high-statistics tritium datasets described in Ref. [59]. The light and charge yields in simulations are tuned to reproduce the tritium data. A comparison between the tuned simulation and the tritium data is shown in Fig. ***
Insert comparison plot here.

1. Implications for NEST ER model – Matthew - Last update 06-15-2015

Because position-dependent pulse area corrections are applied based on ^{83m}Kr data, they are affected by the non-uniformity of the field. In principle this would not be a problem if the light and charge yields for events in the WIMP search region had same dependence with field as ^{83m}Kr events. Unfortunately, at lower energies the light and charge yields are less sensitive to field. This results in a systematic uncertainty on the S2 corrections which can be calculated by comparison to tritium data, and stands at 4% at the center of the detector. The effect on the S1 signal less than 2% at any location in the detector.

F. Nuclear-recoil response – Kevin/Carmen

1. DD neutron calibration – Carmen - Last update 07-06-2015

Mono-energetic neutrons from a deuterium-deuterium (DD) fusion source were used to measure the response of the LUX detector in S_{1c} and S_{2c} to nuclear recoils in the ranges 1.2–14 keV and 0.7–16 keV, respectively [60].

*** Include NR band plot comparing data and simulations.

*** Brief description of the method we use for NR calibration and reference to the DD paper. (We will reference charge and light yield plot, but not duplicate them in this paper).

a. *Modeling Nuclear Recoils in Liquid Xenon* Building and constraining the nuclear recoil response model follows the procedure described in [61]. An energy deposit E_0 in the liquid is distributed between the formation of excitons and formation of electron-ion pairs. Some energy is additionally lost as unmeasurable dissipation of heat. The process is modeled with a modified Platzman equation for rare gases [57], to which an efficiency factor L is applied to account for the energy lost to atomic motion rather than the detectable electronic channels:

$$E_0 = \frac{(N_{ex} + N_i)W}{L} \quad (4)$$

below the LUX liquid surface is known. Uncertainty in the location of the liquid level between the gate grid and the anode leads to uncertainty in the electric field, such that a precise comparison is not possible. The COM4224 SOL field model described in VC3 indicates that the observed value of ϵ_{ee} is consistent with measurements from Ref. [47, 48] for a liquid level 3.6 mm above the gate grid. Such a liquid level is consistent with expectations based upon the design of LUX and uncertainties in the thermal expansion coefficients of the TPC insulators.

We cross-check these results by fitting tritium data to the tritium beta spectrum and find $g_1 = 0.115 \pm 0.005$ and $g_2 = 12.1 \pm 0.9$, implying $\epsilon_{ee} = 0.491 \pm 0.032$. These

where W is the average energy required to produce a quantum (either an exciton or ion) in the liquid. We assume $W = 13.7$ eV.

Three different stages determine how the generated quanta are divided into the final light (S1) and charge (S2) signals. At the first stage, we define a fixed exciton-to-ion ratio N_{ex}/N_i , that determines how much of the energy initially goes to excitation vs. ionization. At the second stage, the ion-electron pairs recombine with probability r to produce further excitons. At the third stage, biexcitonic collisions cause some excitons to de-excite either through heat or through Penning ionization. This effect is modeled by multiplying the resulting number of photons by a fraction f_l , and allowing some fraction P of the quenched excitons to become ions. At the end of these three stages, the leftover excitons de-excite to produce scintillation photons, while the electrons that escape recombination contribute to the charge signal. The final equations for the number of photons (n_{ph}) and electrons (n_e) produced by an energy deposition E_0 are

$$n_{ph} = L \times f_l \times \frac{E_0}{W} [1 - A(1 - r)] \quad (5)$$

$$n_e = L \times \frac{E_0}{W} [B(1 - A)(1 - r) + A] \quad (6)$$

where $A = 1/(1 + N_{ex}/N_i)$ and $B = P(1 - f_l)$.

The L factor The L factor determines the fraction of energy in a nuclear recoil event that goes into scintillation and ionization, rather than atomic motion. In a single Xe-Xe collision, this fraction is given by $s_e/(s_e + s_n)$, where s_e and s_n are the electronic and nuclear stopping powers. Then L represents this fraction for the entire cascade of collisions in an ionization event. We use the model given by Lindhard's theory, with

$$L = \frac{k g(\epsilon)}{1 + k g(\epsilon)} \quad (7)$$

where k is a proportionality constant between the velocity of the recoiling nucleus, and $\epsilon = 11.5(E_{nr}/\text{keV})Z^{-7/3}$ is a dimensionless energy scale. The function g models the ratio of electronic to nuclear stopping powers under the Thomas-Fermi approximation, and is given by

$$g(\epsilon) = 3\epsilon^{0.15} + 0.7\epsilon^{0.6} + \epsilon \quad (8)$$

We treat k as a free parameter when fitting this model to the nuclear recoil data.

In addition to Lindhard's theory, we investigate an alternative model that is more optimistic at energies below 2 keV. We replace the Thomas-Fermi approximation with Ziegler et al.'s parameterization of the nuclear stopping power, as described in [62]. Ziegler's expression is

calculated using the universal screening function. The stopping powers in this model are given by

$$s_e(\epsilon) = 0.166\epsilon^{0.5} \quad (9)$$

$$s_n(\epsilon_Z) = \frac{\ln(1 + 1.1383\epsilon_Z)}{2[\epsilon_Z + 0.01321\epsilon_Z^{0.21226} + 0.19593\epsilon_Z^{0.5}]} \quad (10)$$

where $\epsilon_Z = 1.068\epsilon$. The slight difference in energy scales is due to different assumed screening lengths in the calculation of the dimensionless energy. Following [62], we introduce an additional prefactor α , which multiplies the entire expression to account for the cascade of collisions generated by a single initial nuclear recoil. Thus, $\alpha > 1$. The final expression for the L-factor under the alternative model is

$$L = \alpha \frac{s_e}{s_e + s_n} \quad (11)$$

The Lindhard model (Eq. 7) is used in the signal model to set the WIMP-nucleon cross section limit, while the alternative (Eq. 11) is used merely to demonstrate the effect of more optimistic assumptions in yields at low energies.

Recombination The probability of recombination r is calculated using the Thomas-Imel box model [63], which gives

$$r = 1 - \frac{\ln(1 + N_i \varsigma)}{N_i \varsigma} \quad (12)$$

The energy dependence in this equation is contained in the number of ions N_i . The quantity ς is dependent on the applied electric field. However, LUX is operated and calibrated at a constant 180 V/cm, so these data provide no constraint on this property. We therefore ignore the field dependence in this work and treat ς as a constant parameter.

Biexcitonic collisions A final quenching and ionization is applied to the light signal to account for Penning effects, in which two excitons can interact to produce one exciton and one photon [64], or one photon and one electron. Both processes remove quanta from the photon signal, and this quenching is parametrized by the fraction derived from Birk's saturation law:

$$f_l = \frac{1}{1 + \eta s_e} \quad (13)$$

where η is a strength parameter and s_e is given by Eq. 9. Here f_l represents the proportion of excitons that remain; the fraction of quenched quanta is given by $(1 - f_l)$. This expression exhibits an increased quenching effect with increasing energy, due to higher excitation density along the track of the recoiling Xe atom. Penning ionization is represented by some fraction of the collisions resulting in the release of electrons. We introduce a parameter P to model the unknown ratio of energy lost to ionization vs. heat in biexcitonic processes.

b. Constraining the model To fit the model, we construct a global likelihood that is simultaneously constrained by measurements of the light yield, charge yield, and nuclear recoil band mean. The yields are constrained by an analytical model, while the nuclear recoil band requires a full MC simulation to generate the S1 and S2 signals from which the mean $\log_{10}(S2/S1)$ is calculated in bins of S1. The global likelihood can be separated into the product

$$\mathcal{L}_{global} = \mathcal{L}_{yields} \times \mathcal{L}_{band} \quad (14)$$

The likelihood function for light and charge yields is constructed by assuming each point is a 2D gaussian distribution in energy and yield, with the width given by the x and y uncertainties. Then we calculate a joint likelihood using Eq. 4.1 in [?]:

$$\mathcal{L}_{yields}(\vec{\theta}|E_i, Y_i) = \prod_{i=0}^n \int_0^\infty A_i \exp\left(\frac{-(E_i - E)^2}{2\sigma_{E_i}^2}\right) \times \exp\left(\frac{-(Y_i - \mu_Y)^2}{2\sigma_{Y_i}^2}\right) dE \quad (15)$$

where A_i is a normalization constant, E_i is the energy of the point i , Y_i is either charge or light yield (L_y or Q_y) of point i , and μ_Y is the model prediction at the energy E . The vector $\vec{\theta}$ is the vector of free parameters in the model.

The likelihood for the band mean is constrained by the mean values of $\log_{10}(S2/S1)$ in the nuclear recoil data, binned by S1. We run a full MC simulation of the NR band using the model defined by $\vec{\theta}$ and calculate mean values in the same S1 bins to compare to data. The likelihood equation is given by

$$\mathcal{L}_{band}(\vec{\theta} | \overline{\log_{10}(S2/S1)}_j) = \prod_{j=0}^m B_j \exp\left(\frac{-\left(\overline{\log_{10}(S2/S1)}_j - \mu_{sim}\right)^2}{2(\sigma_j^2 + \sigma_{sim}^2)}\right) \quad (16)$$

In the above, B_j is a normalization constant; $\overline{\log_{10}(S2/S1)}_j$ is the measured band mean in the j th S1 bin, σ_j is the measured uncertainty. The values for μ_{sim} and σ_{sim} are the band mean and uncertainty calculated from the simulation. Due to the need to run the simulation repeatedly while constraining the model, the simulation was run with limited statistics, comparable to the measured values.

To optimize our model, we use a Metropolis-Hastings MCMC algorithm to produce 10,000 samples of $\mathcal{L}_{global}(\vec{\theta})$. The advantage of this method is that it maps out the likelihood distribution across all parameters, so it naturally incorporates correlations. In order to extract an optimal model and uncertainties, we use the

TABLE III. Means and standard deviations of the free parameters using both the Lindhard and the alternative model, calculated from MCMC sample set.

Parameter	Best Fit (Lind)	σ	Best Fit (alt)	σ
k	0.1735	± 0.0060	N/A	N/A
α	N/A	N/A	2.212	± 0.081
ς	0.0168	± 0.0020	0.0145	± 0.0018
N_{ex}/N_i	0.482	± 0.069	0.487	± 0.058
η	13.2	± 2.3	6.7	± 3.4

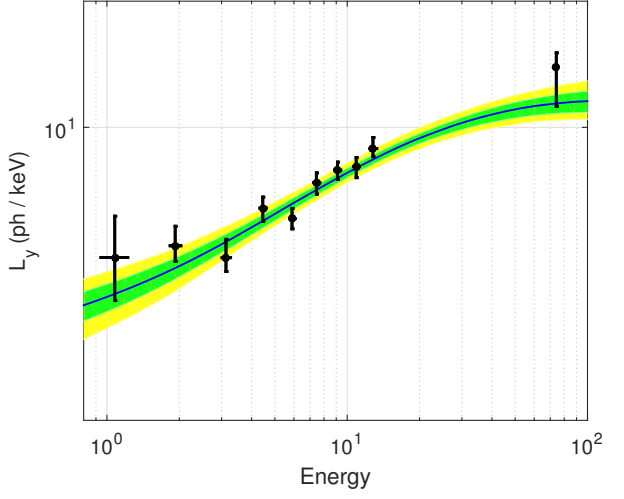


FIG. 38. **PLACEHOLDER** Light yield from model, with DD data overlaid. The the 68% (green) and 95% (yellow) confidence bands are calculated from the MCMC sample set, as described in the text. Also shown (red points) are measurements of the light yield from [65], [66], [67], [68], [69], and [70]. These points are not included in the fit, and are only shown to compare to the extrapolated model.

MCMC sample set to calculate the means and standard deviations of each of the five parameters. The results are shown in Table III. We also construct 68% and 95% confidence bands on the model, shown in figures 38 and 39.

G. Discrimination – Alex L - Last update 09-17-2015

The observed discrimination between electronic and nuclear recoil events was $(99.80 \pm 0.03(\text{stat}) \pm 0.10(\text{sys}))\%$, for events inside the fiducial volume and with an S1 smaller than 50 phd. This means that, on average, one ER event in 500 has a $\log(S2/S1)$ smaller than the NR mean obtained in the NR calibration (see Section V F 1), and thus cannot be distinguished from a NR event produced by a WIMP. This discrimination was estimated by

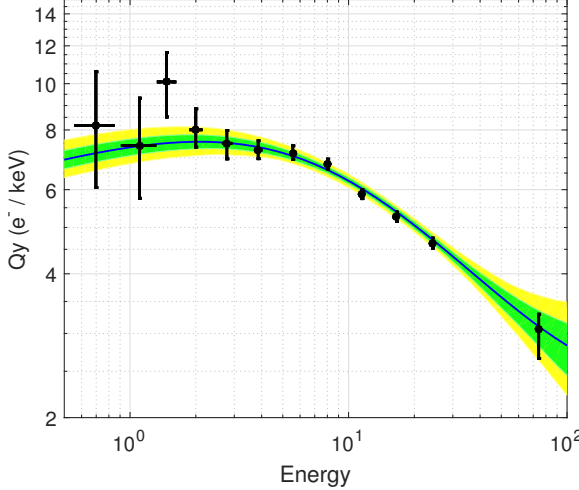


FIG. 39. PLACEHOLDER Charge yield from model, with DD data overlaid. The the 68% (green) and 95% (yellow) confidence bands are calculated from the MCMC sample set, as described in the text. Also shown (red points) are measurements of the charge yield at similar electric fields from [?] and [71]. These points are not included in the fit.

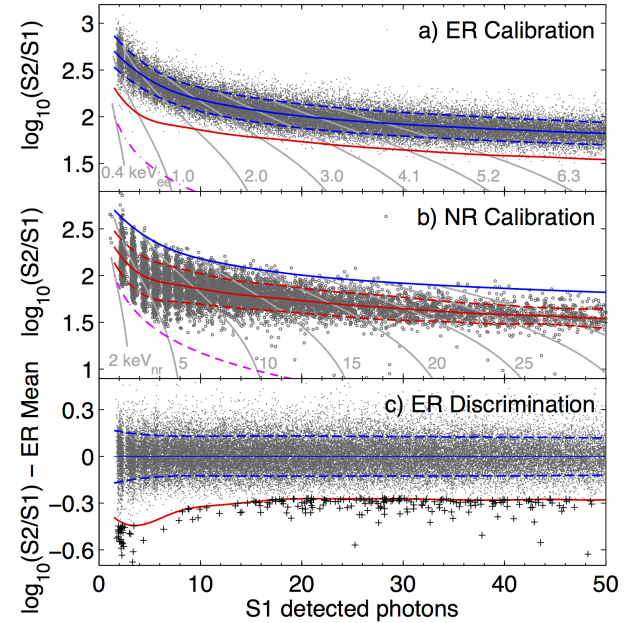


FIG. 40. Calibrations of the detector response in the fiducial volume, and leakage of ER events below the NR mean. Panel *a*) shows the ER (tritium) calibration, while panel *b*) shows the NR calibration (obtained with mono-energetic neutrons from a DD generator). Solid lines show band means, while dashed lines indicate the $\pm 1.28\sigma$ contours (blue for ER and red for NR). Also shown is the S2 threshold applied in the analysis (dot-dashed magenta line). Panel *c*) shows $\log(S2/S1)$ normalised to the mean of the ER band as a function of the $S1$ for the tritium data. The 248 events that fall below the NR mean are plotted using a different marker (plus sign) for clarity.

counting the number of β^- decay events in a large tritium data set ($\sim 150,000$ events in the fiducial region) that fall below the NR mean.

The tritium data used is shown in Figure 40 *c*). The 248 events below the NR mean are represented by a different marker for clarity. The ER band width is represented by the dashed lines, and is mostly flat for $S1$ larger than 5 phd with a small broadening below this value. The difference in $\log(S2/S1)$ between the NR and ER means, shown in full lines in the different panels of Figure 40, has a significant variation below 20 phd resulting in a large dependency of the discrimination on $S1$.

To estimate the discrimination as a function of $S1$, the leaking events were sliced in 3.3 phd wide bins with the first slice centred at 3.35 phd and the last at 49.55 phd. This ensures enough statistics in each bin to estimate the leakage fraction – defined as the ratio between the number of leaking events and the total number of tritium events observed in each bin – while maintaining consistency with the slicing used in both the NR and ER calibrations. The results are shown by black squares in Figure 41. One can see that (with the exception of the first bin) the leakage fraction increases with $S1$ up to ~ 20 phd and remains constant thereafter. The red circles in the same figure represent the leakage fraction obtained from a pure gaussian extrapolation: in this case gaussian fits to the ER band slices are used to get the band width as function of the $S1$, which is then used to estimate the number of events that are below the NR mean. For the first bin, this gaussian estimate underpredicts the observed leakage due to events from below the threshold.

for which the $S1$ fluctuated upwards: these events have relatively smaller S2s, and will thus end up well below the ER band.

The dashed line in Figure 41 is the weighted average of the leakage, in which the weights are the number of events in the WIMP search data for each $S1$ slice. The statistical uncertainty takes into account the uncertainty from the NR calibration and the binomial uncertainty from the number of the leaking events, while the systematic uncertainty is dominated by the field variations along the drift time – resulting in changes in the discrimination between different z positions in the chamber –, with a smaller contribution coming from the variation of the single electron size between the NR and ER calibrations.

Considering the number of ER events in the WIMP search run after quality and fiducial cuts are applied, the expected leakage below the NR mean is $0.7 \pm 0.1(\text{stat}) \pm 0.3(\text{syst})$ events.

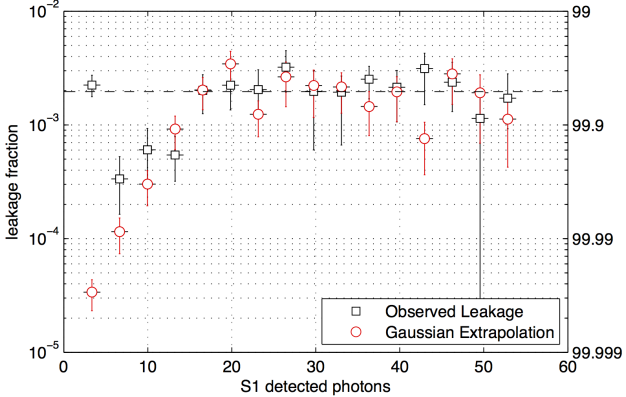


FIG. 41. Leakage fraction (left axis) and discrimination¹⁴⁸⁰ (1-leakage fraction, right axis) as a function of S1. Values¹⁴⁸¹ obtained from a gaussian extrapolation (red circles) are shown¹⁴⁸² along with those obtained from counting β^- decay events in¹⁴⁸³ tritium data. The dashed line corresponds to the average¹⁴⁸⁴ discrimination of 99.80 %.

H. Calibrations for S2-only – Aaron

*** S2 only analysis may not be completed on time to⁴⁹⁰
be included in the PRD paper.

VI. DATA ANALYSIS

A. Event selection: analysis cuts – Alex L - Last update 08-03-2015

We have analyzed data acquired between April 21st⁴⁹⁹ and September 1st 2013, for a total of 132 calendar days⁵⁰⁰ of which 101 days correspond to the data sample for⁵⁰¹ WIMP search. The non dark matter data samples corre⁵⁰²spond to ER and NR calibrations, xenon circulation out⁵⁰³ages and two periods in early August following tritiated⁵⁰⁴ methane injections (due to a higher electron recoil back⁵⁰⁵ground following tritium injections, the data was con⁵⁰⁶servatively excluded from the final analysis). The final⁵⁰⁷ live-time for the actual dark matter search corresponds⁵⁰⁸ to 95 days, which accounts for exclusions due to periods⁵⁰⁹ of detector instability (2.5 %), the trigger hold-off (1.8 %)⁵¹⁰ and other minor contributions (lost/corrupted files and⁵¹¹ DAQ dead-time (1.6 %)).

Single scatter events (dubbed golden events), repre⁵¹²sentative of WIMP elastic scattering off nuclei, are se⁵¹³lected for further analysis (see Section III D 2). Monitor⁵¹⁴ing of the detector stability was done using slow control⁵¹⁵ (SC) parameters that could influence its response: liquid⁵¹⁶ level, HV grid voltages and currents, outer vacuum vessel⁵¹⁷ pressure, circulation flow rate and detector pressure. All⁵¹⁸ these parameters were scanned for the entire duration of⁵¹⁹ the run looking for out-of-bounds periods, with excurs⁵²⁰ions occurring less than 5 min apart being merged into⁵²¹ a single unified period. Zero length outages (a single data⁵²²

point outside bounds) were extended to the past and the future by the average of the update period for the corresponding SC sensor in the 10 min interval containing the excursion. Zero length outages were not considered for the liquid level and the outer vacuum pressure, as they would likely be caused by sensor fluctuations; all other outages resulted in data being excluded from the analysis. An outage is considered to be over once the sensor is back into bounds, with the exception of circulation failures: in this case the outage period is extended until the next ^{83m}Kr calibration, which provides information about the electron lifetime. Additionally, the trigger rate of each dataset was visually inspected and periods of 30 sec around the rate excursions were excluded from the final analysis.

A radial fiducial cut was placed at 20 cm, driven by the leakage of decay products from Rn daughters implanted on the detector walls as discussed in Section VI C 2. Additionally, the height of the fiducial volume was defined from 38 to 305 μs in drift time (corresponding to a total liquid height of 40.3 ± 0.2 cm) to reduce backgrounds from the PMT arrays and electrodes. Finally, the S1 and S2 thresholds (1 phd and 150 phd respectively, described in detail in Section VI B) were applied to the remaining events, as well as an S1 upper limit of 50 phd.

The cleanliness of the data acquired allowed for an analysis with only a single data quality cut, to exclude periods of high rate of single electron background. Small S2 pulses due to single electrons leaving the liquid surface are prevalent in the extended tails of genuine high energy events (for up to several ms), and may exceed the S2 threshold either due to a fluctuation in a single electron signal size, or more commonly due to multiple electrons leaving the liquid within few μs . These S2s may be associated with a random isolated S1 or a fake S1 resulting from the pulse finder algorithm over-splitting a prior single electron and produce a fake event. Excluding events with a significant area outside the (S1 and S2) signal pulses effectively removes these fake events while ensuring a large acceptance for WIMP-like events.

Figure 42 shows golden events from the WIMP search data plotted as a function of the total raw signal area ($S_1 + S_2$ areas) and the extra (non-signal) area contained within the same event. The dashed line indicates the threshold for the maximum allowed non-signal area in an event, starting at 80 phd (which corresponds to ~ 3 extracted electrons) per 1 ms event window for small energy deposits and slowly increasing from this value for events with a total signal area above 630 phd. The associated acceptance was determined by slicing randomly chosen background datasets in 1 ms time windows and evaluating the total area contained within. The top plot in Figure 43 shows the distribution of cumulative areas inside these 1 ms intervals in one of the tested datasets, with 99% of the windows containing less area than the 80 phd value used in the cut. This value was confirmed using tritium calibration data for signal areas above 400 phd (see bottom plot in Figure 43), with the cut excluding

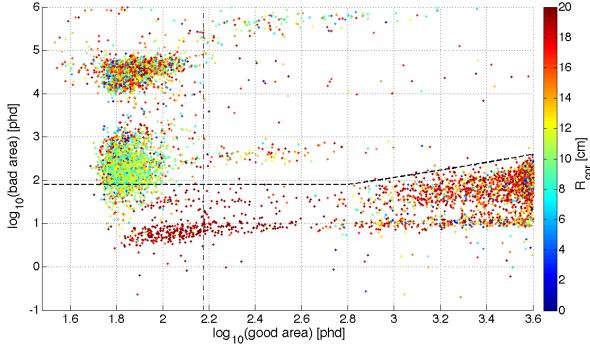


FIG. 42. Cleanliness cut (shown by the dashed lines) – which removes periods of high-rate single electron background – defined as a function of extra non-signal area contained within the 1 ms window of each event. The 150 phd S2 threshold used in the analysis is also shown (vertical dot-dashed line). The data points representing the golden single scatter events are colour coded according to their radial position in the detector.

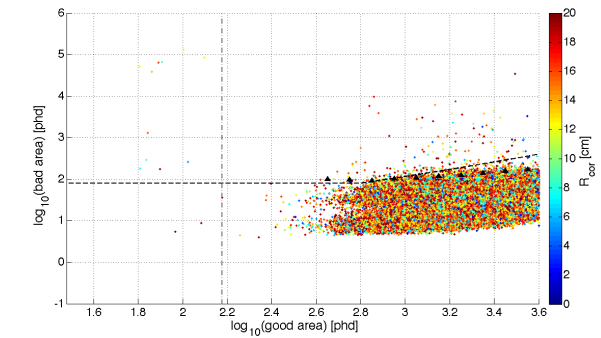
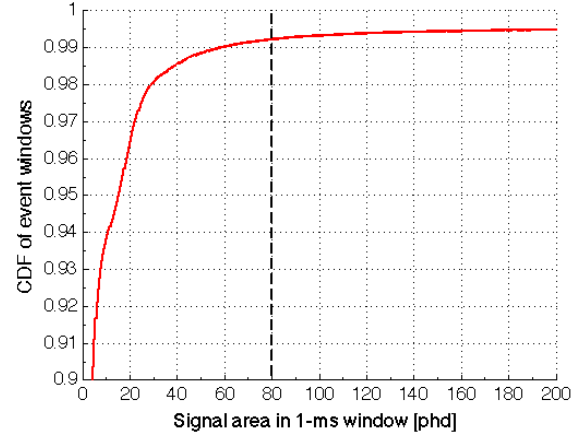


FIG. 43. **Top:** Cumulative number of 1 ms time window slices from a randomly picked WIMP search dataset as a function of the event area contained within, showing 99% acceptance at 80 phd. **Bottom:** Cleanliness cut (dashed lines) applied to a tritium calibration dataset, confirming an acceptance of $\gtrsim 99\%$ for good areas above 400 phd (black triangles indicate the 99% percentile in each good area bin; the vertical dot-dashed line shows the 150 phd S2 threshold).

less than 1% of the events in all signal area bins.
Table IV summarises the effect of each of the analysis cuts and thresholds applied to the WIMP search data in the number of events acquired during Run 3.

Cut	Events remaining after cut
All triggers	93126362
Single scatters	5375716
Stability cuts	5221580
Fiducial volume	1923367
S1 range (1 – 50 phd)	6898
S2 threshold (>150 phd)	840
Cleanliness cut	590

TABLE IV. Effect of each of the event level cuts on the total number of acquired WIMP search triggers

B. Efficiency and threshold – Alex L - Last update 06-15-2015

1. S1 threshold

The S1 threshold is applied on the fully xyz-corrected number of spikes, whose minimum is restricted by the 2-fold coincidence requirement in the S1 definition implemented in the pulse classification module (see section III D 1). As a result of position corrections, S1s smaller than 2 detected spikes are possible despite the two-fold coincidence, but in the original analysis [?] an additional 2 phe threshold was imposed. Closer investigation of the region below this threshold did not reveal any additional noise or unexpected populations, and

it was thus decided to lower the S1 threshold to 1 phd for this analysis — doing so increases the detection efficiency for S1s by 25% (!!!get updated number!!!) at 3 keVnr relatively to the previous threshold (see Fig. 44). The fully integrated background model (described in Sec. VI C), including contributions from the cosmogenically activated ^{127}Xe which limited the upper bound of the S1 scale to 30 phe in the original analysis, allows the extension of the upper limit to 50 phd. As described in Sec. VI C 2, S1s above 50 phd (outside the region of interest for the WIMP search) were used to estimate the leakage of wall events into the fiducial volume.

2. S2 threshold

The threshold on the S2 signal is applied on the uncorrected raw pulse areas, and is driven by the definition of the fiducial volume and the power of the cleanliness cut to exclude events during periods of high rate single

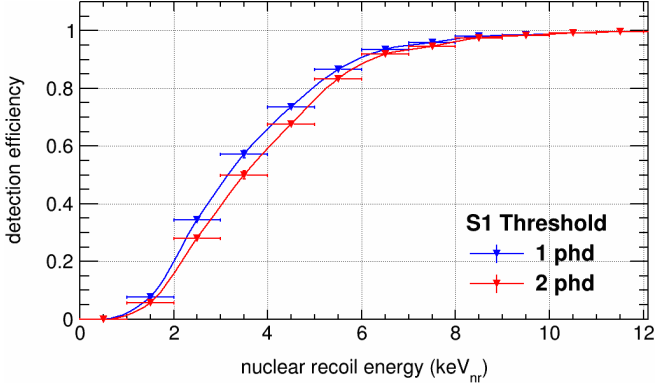


FIG. 44. Detection efficiency of S1 signals calculated from a background free nuclear recoil simulation with a flat energy spectrum for different thresholds within a fiducial volume of 18 cm.

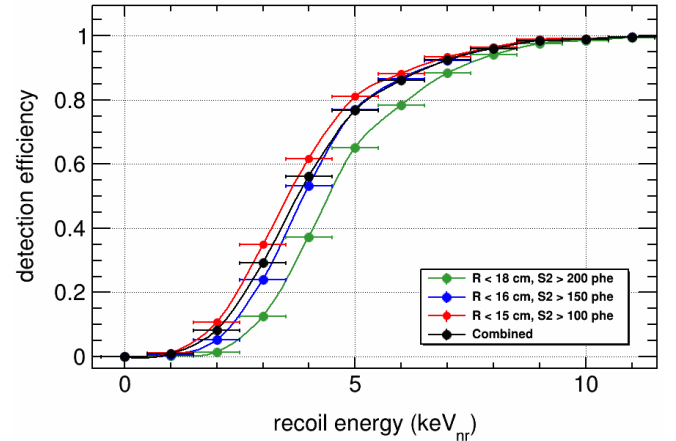


FIG. 45. PLACEHOLDER only. Final plot should have S2 only efficiency and s1+s2 efficiency

1558 electron background following large S2 signals. 1559

Over a broad range of energies, events occurring close 1560 to the detector walls may be wrongly reconstructed inside 1561 the fiducial volume due to incomplete charge collection 1562 and be mistakenly identified as WIMP like signals. Con- 1563 sidering these events behave in a similar manner for dif- 1564 ferent S1 regions for small sized S2 signals, their expected 1565 leakage into a given fiducial volume in the S1 WIMP 1566 search range of interest ($S1 < 50$ phd) can be estimated 1567 for different S2 thresholds using events from the WIMP 1568 search data with an S1 greater than 50 phd (see Sec- 1569 VIC 2 for more details on this study). 1604

Ultimately the S2 threshold was set at 150 phd, de- 1570 termined by the capability of the cleanliness cut to re- 1571 move events in periods of high rate single electron back- 1572 ground in which fake S2s can be paired with coinci- 1573 dent single photoelectrons or S1s from dead-regions of 1574 the detector, and the very low efficiency for events with 1575 $100 < S2 < 150$ phd that still have a valid S1, as shown in 1576 Fig. 45. 1607

3. Efficiencies

*** This section is still waiting for re-analysis to be completed

Efficiencies are calculated utilising a variety of meth- 1615 ods. ER detection efficiencies are calculated from the 1616 tritium calibration data sets using a purely data driven 1617 approach. NR efficiencies are calculated from AmBe 1618 calibration data by comparing data to the output from 1619 the full LUX simulation. 1620

When extracting efficiencies from calibration data the 1622 resulting data histograms are normalised above some en- 1623 ergy ($>??$ phd in S1) to the expected spectra. This 1624 threshold is well above the point when efficiency hits 1625 unity from purely simulation driven flat nuclear recoil 1626

efficiency studies (see Fig. ?? - possibly in PLR paper?). However, to ensure that all pulse topologies occurring in the data, as well as potential losses due to the restriction to 10 recorded pulses in the DPF, are covered in our efficiency estimation, an absolute DPF efficiency has been determined from the 4000 NR calibration hand scanned events (see section Event classification). In this instance a list of golden single scatter events, which have been identified by manual scanning, are compared to the output of the DPF. Applying all analyse cuts, it was found that >97% of all golden events have been successfully captured and identified by the LUX DPF.

C. Backgrounds – Alastair - Last update 06-15-2015

1. Coincidence background

Apparent golden events can be generated by the ran- 1608 dom coincidence, in order and within a drift-time, of an 1609 S1-only event and an S2-only event. Apparent S1-only 1610 events, i.e. a minimum of two PMTs recording a photo- 1611 electron within 100ns of each other without an accom- 1612 panying S2, may be caused by energy deposition in the 1613 sub-cathode dead region, random coincidence of dark- 1614 count photoelectrons, or Cerenkov light (emitted, for ex- 1615 ample, in PTFE components or the window of a PMT). 1616 S2-only events are caused by low-energy tracks in an S2- 1617 live volume, i.e. the drift or extraction regions, which 1618 generate fewer than two detected S1 photons. The z 1619 position inferred from apparent drift time in these events 1620 is a uniform random variable, so they constitute a back- 1621 ground even in large xenon TPCs where conventional sin- 1622 gle scatters from peripheral radioactivity are excluded by 1623 the fiducial volume. 1624

In order to contribute to the coincidence background, an S2 must have raw area above the 150 phd analysis

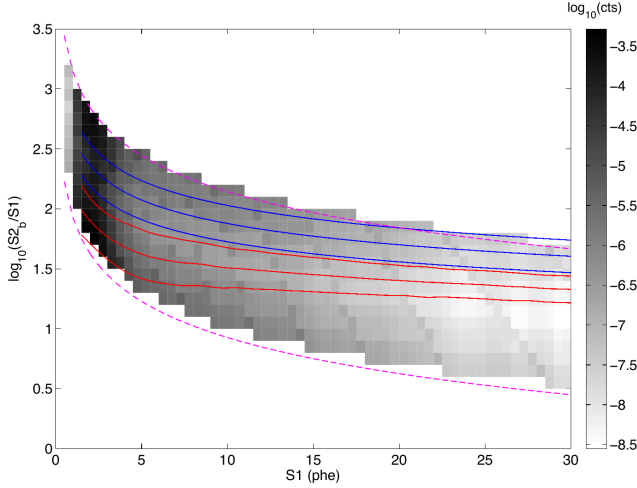


FIG. 46. PLACEDHOLDER Distribution in S1, S2 of events caused by random coincidence S1-only and S2-only events

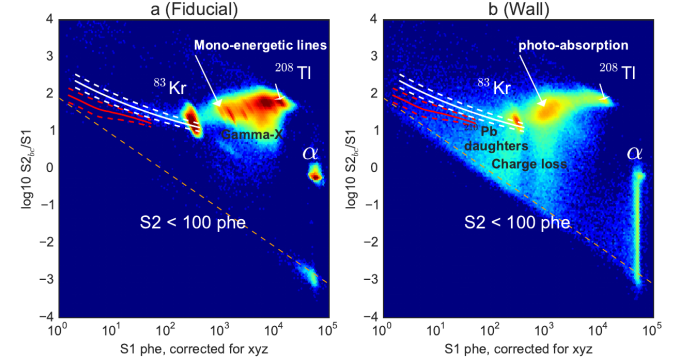


FIG. 47. Distribution in S1, S2 of background events at radii consistent with the wall (b) compared with the inner 15 cm (a), illustrating incomplete charge collection close to the PTFE walls. (From Ref.[72])

threshold, be reconstructed within the fiducial radius, and occur in an event window which passes the cleanliness cut and contains no preceding S1. The spectrum of S2s meeting these criteria was obtained from a representative sample of WIMP search datasets. The isolated S2 rate from threshold to 4500 phd raw area—covering the entire NR signal region—is 5 mHz. Beta particles and alpha-decay daughter nuclei originating on the wires of the gate electrode are a common cause of S2-only events due to the high field and the obscuration of S1 light; the characteristic short duration of gate S2s, for which the electron cloud diffuses very little in z on the way to surface, could be used to reduce this background at some penalty in efficiency, though this was not required for the LUX S1-S2 WIMP search.

Trigger efficiency for S1s rolls off to zero in the search range (below 50 phd) but, because all samples passing zero-suppression are written to disk by the DAQ, the rate of isolated S1s can still be measured by applying the pulse-finder algorithm to representative WIMP search data, irrespective of the trigger. The isolated S1 rate from threshold to 50 phd raw area is 1 Hz, with a falling spectrum. Figure 46 shows the resulting distribution of background events due to coincidence S1-only and S2-only events, which leads to a prediction of 1.1 background events in the 95.0-day Run 3 reanalysis sample.

2. Nuclear-recoil and surface backgrounds

Nuclear recoils contributing to the WIMP background in LUX can be caused by elastic scattering of fast neutrons or by surface alpha decays in which the daughter nucleus recoils into the liquid xenon target. Neutron background rates are estimated in detail in Ref. [34] and contribute a negligible expectation of 0.08 events in the

enlarged fiducial volume and longer exposure of the Run 3 reanalysis.

The efficiency for ionized charge to drift to the electroluminescence region is lower for tracks at the PTFE surface than for those in the liquid xenon bulk. This partial charge collection is seen in data as a suppressed and variable S2 yield for Kr-83m and tritium calibration events reconstructed at radii consistent with the wall. Search-data events at high r exhibit the same effect, with S2 distributions extending from the bulk-liquid ER band right down to threshold throughout the S1 range of interest. Figure 47 shows the resulting broad distribution of reconstructed light and charge.

Wall events constitute a background to WIMP search only when reconstructed inside the fiducial radius. The suppressed $S2/S1$ ratio described above tags wall events without reference to their reconstructed radius, allowing one to model the resolution of the wall in r empirically with a high- $S1$, low- $S2/S1$ sideband away from the WIMP signal region. The low- r side of the resolved wall is well described by an S2-dependent Gaussian distribution with standard deviation

$$\sigma[r\text{[cm]}] = \frac{1}{0.61 \log_{10}(S2c[\text{phd}])} \quad (17)$$

The rate and S1-S2 distribution of the wall background were derived from the data themselves, non-parametrically. X-rays, Compton scatters and daughter Pb-206 nuclei recoiling against undetected alpha particles all contribute to the wall population, but their signal yields are not readily simulated. Instead, an empirical wall radius was calculated, for each bin of polar angle, from the median radius of the extreme low-S2/S1 population, and kernel density estimation was applied to all events beyond this radius to construct a wall PDF in S1, S2. Multiplying by the Gaussian conditional distribution for r given $S2$ results in the complete model for wall events in the fiducial volume, shown in Figure 48, and a prediction of 24 ± 7 counts in the 95.0-liveday sample.

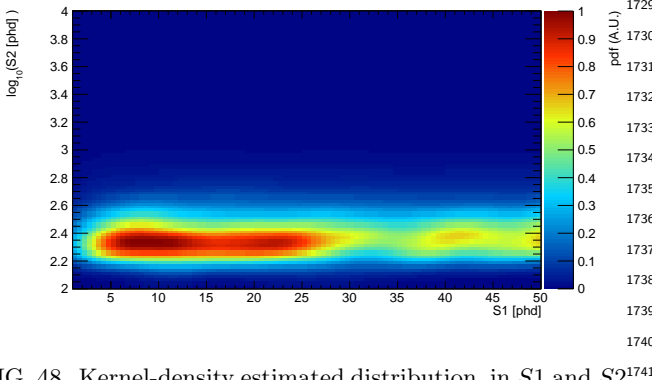


FIG. 48. Kernel-density estimated distribution, in S_1 and S_2 ,¹⁷⁴¹ of wall background events reconstructed within the fiducial¹⁷⁴² volume. The predicted count is 24 events within the 145-kg¹⁷⁴³ fiducial volume over 95.0 livedays.

rameters (BiExA) which accounts for the Penning effects ¹⁷²⁹. At this step, we have the final number of photons and number of electrons models near the site of the interaction. The photons are directly detected by our PMT as S_1 . The parameter g_1 accounts for our photon detection efficiency of these photons which is also allowed to vary in NEST. The final parameter is g_2 , which is a combination of the extraction efficiency of the electrons and our scintillation light detection efficiency in the gas phase of the detector. These are parameters values and uncertainties are listed on table III on V F 1 b with the additional parameters from our calibration data $g_1 = 0.120 \pm 0.002$ and $g_2 = 10.9 \pm 0.4$ [59].

As with all other models within the Profile Likelihood Ratio (PLR), the signal model is constructed with an amplitude and Probabilities Distribution Function (PDF) shape.

$$\text{SigModel} = \text{SigAmp}(\Theta_A) \times \text{SigPDF}(Obs, \Theta_B) \quad (18)$$

3. Electron-recoil backgrounds

¹⁶⁹⁸ How PLR models are built. How background models¹⁷⁴⁷ inform choice of FV.
¹⁶⁹⁹

¹⁷⁰⁰ **D. Signal model – Carmen - Last update**
¹⁷⁰¹ **06-30-2015**

¹⁷⁰² The limits shown in this paper are based upon two theoretical¹⁷⁵⁴ model for dark matter. These are the spin independent¹⁷⁵⁵ (SI) and spin dependent (SD) weakly interacting¹⁷⁵⁶ mass particles (WIMP). The SI WIMP signal model follows¹⁷⁵⁷ the prescription from Lewin and Smith [73]. The SI¹⁷⁵⁸ WIMP recoil energy spectrum is shown on ?? for various¹⁷⁵⁹ WIMP masses. While the SD WIMP signal model¹⁷⁶⁰ is based upon P. Klos et al. [?]. The recoil energy¹⁷⁶¹ spectrum from these models are used to translate the¹⁷⁶² theoretical model into LUX observables using the Noble¹⁷⁶³ Element Simulation Technique (NEST). NEST is a model¹⁷⁶⁴ for nuclear recoil in liquid Xenon, which is described in¹⁷⁶⁵ detail in the NEST model section IV A.

¹⁷⁶⁶ **1. Spin-Independent Signal Model**

¹⁷⁶⁷ For the SI WIMP signal model, NEST contains seven¹⁷⁷¹ different model parameters which are allowed to vary in¹⁷⁷² the signal Model. L factor (α_L) determines the fraction¹⁷⁷³ of the recoil energy which is converted into scintillation¹⁷⁷⁴ and ionization energy. The Exponential low energy suppression term ($a_{expSupp}$) which allows the L factor to tend¹⁷⁷⁶ towards zero as the recoil energy goes to zero. The ratio between the number of exciton and ions which determines¹⁷⁷⁸ amount of initial ratio of excitation quanta over ionization¹⁷⁷⁹ quanta (N_{ex}/N_i) before recombination. The recombination probability is calculated by the Thomas-¹⁷⁸¹ Imel box model ?? which contains a parameter we call¹⁷⁸² TIB. The fifth parameter is the biexcitonic quenching pa¹⁷⁸³

¹⁷⁴⁸ Θ_A are parameters which change the signal amplitude within our event selection (efficiency \times number of signal events) where Θ_B changes shape of the PDF in S_1 and $\text{Log}_{10}(S_2)$ space. These parameters are those listed above in the NEST model and the fitter does not allow for the same parameter to be in both Θ_A and Θ_B . Obs are the four observables in LUX: S_1 , $\text{Log}_{10}(S_2)$, r and z. The PDF in radius, r, is simply a linear function in r to account for increase in the differential event rate in r. The PDF in Z is taken to be a flat uniform distribution. The PDF in $\text{Log}_{10}(S_2)$ and S_1 is created using NEST as the previous paragraph described. In order to construct physically meaningful limits (the WIMP interaction cross section), *SigAmp* is constructed out of the cross section times the number of events per zeptobarn (*EvtPerZb*) with the analysis fiducial mass and exposure time.

¹⁷⁴⁹ In order to quantify the effects of these nuisance parameters we check the difference each nuisance makes on the *EvtPerZb* and Shape of the PDF in S_1 and $\text{Log}_{10}(S_2)$ by varying them $\pm 1\sigma$ uncertainties. The effect is shown on figures ?? and ?? for a WIMP mass of 5 GeV and 50 GeV respectively. $\Delta(EvtPerZb)$ is the ratio between the $nSig_{variation}/nSig_{nominal}$ after all analysis has been made. X^2/NDF is the Chi sqr per degrees of freedom between a shape with their respective variation and the shape without any variation.

¹⁷⁵⁰ From figure ??, one can see that the parameters which affect the $\Delta(EvtPerZb)$ are g_2 , α_L and a_{Lind} , in order from the largest effect to the smallest. From both ?? and ??, one also sees that g_2 dominates over all other nuisance parameters in its effect on X^2/NDF . Since g_2 affects both the shape and the normalization factor in the signal PDF. It was chosen to allow g_2 vary in the shape of the signal model. The fitting algorithm does not allow for the shape and normalization to depend on the same parameter. α_L and a_{Lind} were chosen for the normalization variation.

TABLE V. Nuisance parameters used in the signal model.

M_{WIMP}	$g1 \pm 1.7\%$	$g2 \pm 8\%$	α_L	TIB	a_{Lind}	N_{ex}/N_i	$BiE_{\gamma\gamma}^{1824}$
5	32	163	14	11	5	11	$25_{\pm 28}^{1827}$
10	85	1081	108	399	26	98	$30_{\pm 30}^{1829}$
50	144	7970	68	1135	74	281	$220_{\pm 32}^{1831}$

The measured cross-sections are therefore on the WIMP-neutron or WIMP-proton cross-section, to allow comparison between detectors of different target materials.

Several spin structure function calculations for the neutron and proton-only cases are available. They differ in which nuclear states are included in the nuclear shell model, the allowed configuration of nucleons in those states, which interactions are included and the internucleon potential used. The calculation used for this analysis is from [?]. It has the largest number of states available, and more allowed states than other work. The potential used has been well tested for other applications. Also, it includes the contribution from two-body currents, which are couplings between the WIMP and two nucleons. With this, even for "proton-only" coupling an interaction including a neutron can occur (and vice-versa). The SD sensitivity is smaller than SI, and the neutron-only sensitivity is greater than the proton-only in Xenon. This is because both of the spin sensitive isotopes have an unpaired neutron, not a proton. However, including the two-body currents gives an enhancement to the proton-only structure while only slightly reducing the neutron-only (relative to only 1-body currents).

The set of possible nuisance parameters is the same as for the SI case, but with two additions. There is a theoretical uncertainty in the spin structure functions for ^{129}Xe and ^{131}Xe . The effect of all the nuisance parameters on the results was assessed in the same way as the SI case. It was again found that only the g2 variation was significant for the shape, and the Lindhart variation for the overall normalisation. Therefore the uncertainties in the structure functions were not included. The results are summarised in table ??.

*** add Nuisance parameters results table: Parameter name, change in overall number of events, change in shape.

The method for calculating the limits in the SD case is the same than for the SI one, but using the differential nuclear recoil spectrum shown in figure ???. As shown in Figure ??, the shape of the spectrum is similar to the SI case, but the overall number of events is much smaller.

*** add plot of recoil spectra for some masses

E. Calculating the limit: PLR – Alastair - Last update 06-15-2015

Statisti

VII. DISCUSSION & OUTLOOK

VIII. ACKNOWLEDGEMENT

1834

1835

1836

1837

1838

1839

1840

1841

1842

1843

1844

1845

1846

1847

1848

1849

1850

1851

1852

1853

1854

1855

1856

1857

1858

1859

1860

1861

1862

1863

1864

1865

1866

1867

1868

1869

1870

1871

1872

1873

1874

1875

1876

1877

1878

1879

1880

1881

1882

1883

1884

1885

1886

1887

1888

1889

1890

1891

1892

1893

1894

1895

1896

1897

1898

1899

1900

1901

1902

1903

1904

1905

1906

1907

1908

1909

1910

1911

1912

1913

1914

1915

1916

1917

1918

1919

1920

1921

1922

1923

1924

1925

1926

1927

1928

1929

1930

1931

1932

1933

1934

1935

1936

1938

1939

1940

1941

1942

1943

1944

1945

1946

1947

1948

1949

1950

1951

1952

1953

1954

1955

1956

1957

1958

1959

1960

1961

1962

1963

1964

1965

1966

1967

1968

1969

1970

1971

1972

1973

1974

1975

1976

1977

1978

1979

1980

1981

1982

1983

1984

1985

1986

1987

1988

1989

1990

1991

1992

1993

1994

1995

1996

1997

1998

1999

1999

1999

1999

1999

1999

1999

1999

1999

1999

1999

1999

1999

1999

1999

1999

1999

1999

1999

1999

1999

1999

1999

1999

1999

1999

1999

1999

1999

1999

1999

1999

1999

1999

1999

1999

1999

1999

1999

1999

1999

1999

1999

1999

1999

1999

1999

1999

1999

1999

1999

1999

1999

1999

1999

1999

1999

1999

1999

1999

1999

1999

1999

1999

1999

1999

1999

1999

1999

1999

1999

1999

1999

1999

1999

1999

1999

1999

1999

1999

1999

1999

1999

1999

- [1] D. N. Spergel *et al.*, *Astrophys. J. Supp. S.* **170**, 377¹⁹³² (2007).¹⁹³³
- [2] W. J. Percival *et al.*, *Astrophys. J.* **657**, 645 (2007).¹⁹³⁴
- [3] P. A. R. Ade *et al.* (Planck Collaboration), *Astron. Astrophys.* **571**, A16 (2013).¹⁹³⁵
- [4] M. W. Goodman and E. Witten, *Phys. Rev. D* **31**, 3059¹⁹³⁷ (1985).¹⁹³⁸
- [5] B. W. Lee and S. Weinberg, *Phys. Rev. Lett.* **39**, 165¹⁹³⁹ (1977).¹⁹⁴⁰
- [6] D. E. Kaplan, M. A. Luty, and K. M. Zurek, *Phys. Rev. D* **79**, 115016 (2009).¹⁹⁴¹
- [7] K. M. Zurek, *Phys. Rept.* **537**, 91 (2014).¹⁹⁴²
- [8] G. J. Alner *et al.* (ZEPLIN-II Collaboration), *Astropart. Phys.* **28**, 287 (2007).¹⁹⁴⁴
- [9] D. Y. Akimov *et al.* (ZEPLIN-III Collaboration), *Astropart. Phys.* **27**, 46 (2007).¹⁹⁴⁵
- [10] E. Aprile *et al.* (XENON10 Collaboration), .¹⁹⁴⁸
- [11] D. S. Akerib *et al.* (LUX Collaboration)¹⁹⁴⁹ *Nucl.Instrum.Meth. A***704**, 111 (2013), arXiv:1211.3788¹⁹⁵⁰ [physics.ins-det].¹⁹⁵¹
- [12] X. G. Cao *et al.* (Panda-X Collaboration), *Sci. China Phys. Mech. Astron.* **57**, 1476 (2014).¹⁹⁵²
- [13] J. B. Albert *et al.*, *Phys. Rev. C* **89**, 015502 (2014).¹⁹⁵³
- [14] A. Gando *et al.*, *Phys. Rev. C* **85**, 045504 (2012).¹⁹⁵⁴
- [15] L. Baudis *et al.*, *J. Cosmol. Astropart. Phys.* **01**, 044¹⁹⁵⁵ (2014).¹⁹⁵⁶
- [16] D. S. Akerib *et al.* (LUX Collaboration), ArXiv e-prints¹⁹⁵⁸ (2015), arXiv:run3.Re-analisis result.¹⁹⁵⁹
- [17] J. Heise, (2015), arXiv:1503.01112 [physics].¹⁹⁶⁰
- [18] D. S. Akerib *et al.* (LUX Collaboration), *Astropart.Phys.* **45**, 34 (2013), arXiv:1210.4569 [astro-ph.IM].¹⁹⁶²
- [19] D. S. Akerib *et al.* (LUX Collaboration), *Phys.Rev.Lett.* **112**, 091303 (2014), arXiv:1310.8214 [astro-ph.CO].¹⁹⁶³
- [20] D. S. Akerib *et al.* (LUX Collaboration), (2011)¹⁹⁶⁵ arXiv:1112.1376.¹⁹⁶⁶
- [21] D. S. Akerib *et al.* (LUX Collaboration), *Nucl. Instrum. Meth. A***709**, 29 (2013).¹⁹⁶⁷
- [22] A. Dobi *et al.*, *Nucl. Instrum. Meth. A***665**, 1 (2011).¹⁹⁶⁹
- [23] A. Dobi *et al.* (EXO Collaboration), *Nucl. Instrum. Meth. A***675**, 40 (2012).¹⁹⁷¹
- [24] D. S. Akerib *et al.* (LUX Collaboration)¹⁹⁷² *Nucl.Instrum.Meth. A***668**, 1 (2012), arXiv:1108.1836¹⁹⁷³ [astro-ph.IM].¹⁹⁷⁴
- [25] D. S. Akerib *et al.*, ArXiv e-prints (2015)¹⁹⁷⁵ arXiv:trigger.paper.¹⁹⁷⁶
- [26] M. Moongwelwan *et al.*, (2015).¹⁹⁷⁷
- [27] V. N. Solovov *et al.*, *IEEE Trans.Nucl.Sci.* **59**, 3286¹⁹⁷⁸ (2012), arXiv:1112.1481 [physics.ins-det].¹⁹⁷⁹
- [28] D. S. Akerib *et al.*, ArXiv e-prints (2015)¹⁹⁸⁰ arXiv:PositionReconstruction.paper.¹⁹⁸¹
- [29] D. S. Akerib, X. Bai, S. Bedikian, E. Bernard, A. Bernstein, A. Bradley, S. B. Cahn, M. C. Carmona-Benitez,¹⁹⁸² D. Carr, J. Chapman, *et al.*, *Nuclear Instruments and Methods in Physics Research Section A: Accelerators, Spectrometers, Detectors and Associated Equipment* **675**, 63 (2012).¹⁹⁸³
- [30] S. Agostinelli, J. Allison, K. a. Amako, J. Apostolakis,¹⁹⁸⁸ H. Araujo, P. Arce, M. Asai, D. Axen, S. Banerjee,¹⁹⁸⁹ G. Barrand, *et al.*, *Nuclear instruments and methods in physics research section A: Accelerators, Spectrometers,*¹⁹⁹⁰ *Detectors and Associated Equipment* **506**, 250 (2003).¹⁹⁹¹
- [31] J. Allison *et al.*, *IEEE Trans.Nucl.Sci.* **53**, 270 (2006).
- [32] M. Szydagis, N. Barry, K. Kazkaz, J. Mock, D. Stolp, M. Sweany, M. Tripathi, S. Uvarov, N. Walsh, and M. Woods, *Journal of Instrumentation* **6**, P10002 (2011).
- [33] M. Szydagis, A. Fyhrie, D. Thorngren, and M. Tripathi, *Journal of Instrumentation* **8**, C10003 (2013).
- [34] D. S. Akerib *et al.* (LUX Collaboration), ArXiv e-prints (2014), arXiv:1403.1299 [astro-ph.IM].
- [35] C. M. B. Monteiro, L. M. P. Fernandes, J. A. M. Lopes, L. C. C. Coelho, J. F. C. A. Veloso, J. M. F. dos Santos, K. Giboni, and E. Aprile, *Journal of Instrumentation* **2**, P05001 (2007).
- [36] A. C. Fonseca, R. Meleiro, V. Chepel, A. Pereira, V. Solovov, and M. I. Lopes, *Nuclear Science Symposium Conference Record, 2004 IEEE* **1**, 572 (2004).
- [37] D. C. Malling, *Measurement and Analysis of WIMP Detection Backgrounds, and Characterization and Performance of the Large Underground Xenon Dark Matter Search Experiment*, Ph.D. thesis, Brown University (2013).
- [38] J. Chapman, *First WIMP Search Results from the LUX Dark Matter Experiment*, Ph.D. thesis, Brown University (2014).
- [39] C. A. B. Oliveira, H. Schindler, R. Veenhof, S. Biagi, C. M. B. Monteiro, J. M. F. dos Santos, A. L. Ferreira, and J. F. C. A. Veloso, *Phys.Rev.B* **703**, 217 (2011), arXiv:1103.6237 [physics.ins-det].
- [40] J. Mock, N. Barry, K. Kazkaz, D. Stolp, M. Szydagis, M. Tripathi, S. Uvarov, N. Walsh, and M. Woods, *Journal of Instrumentation* **9**, T04002 (2014).
- [41] H. M. Araujo *et al.*, *Nucl.Instrum.Meth. A***521**, 407 (2004).
- [42] P. Sorensen, *A Position-Sensitive Liquid Xenon Time-Projection Chamber for Direct Detection of Dark Matter: The XENON10 Experiment*, Ph.D. thesis, Brown University (2008).
- [43] C. Silva, J. P. da Cunha, A. Pereira, M. I. Lopes, V. Chepel, V. Solovov, and F. Neves, *Nucl.Instrum.Meth. A***619**, 59 (2010), arXiv:0910.1058 [physics.ins-det].
- [44] A. Hitachi, V. Chepel, M. I. Lopes, and V. Solovov, *The Journal of Chemical Physics* **123**, 234508 (2005).
- [45] G. M. Seidel, L. R. E., and W. Yao, *Nucl.Instrum.Meth. A***489**, 189 (2002), arXiv:0111054 [hep-ex].
- [46] C. H. Faham *et al.*, (2015), arXiv:1506.08748 [physics.ins-det].
- [47] E. M. Gushchin, A. A. Kruglov, V. V. Litskevich, A. N. Lebedev, I. M. Obodovskii, and S. V. Somov, *Zh. Ebp. Teor. Fiz.* **76**, 1685 (1979).
- [48] E. M. Gushchin, A. A. Kruglov, and I. M. Obodovskii, *Zh. Ebp. Teor. Fiz.* **82**, 1485 (1982).
- [49] E. Aprile and T. Doke, *Rev.Mod.Phys.* **82**, 2053 (2010), arXiv:0910.4956 [physics.ins-det].
- [50] C. Silva, J. P. da Cunha, A. Pereira, V. Chepel, M. I. Lopes, and V. Solovov, ArXiv e-prints (2009), 10.1063/1.3318681, arXiv:0910.1056.
- [51] B. Edwards, H. M. Araujo, V. Chepel, D. Cline, T. Durkin, *et al.*, *Astropart.Phys.* **30**, 54 (2008), arXiv:0708.0768 [physics.ins-det].
- [52] E. Santos *et al.* (ZEPLIN-III), *JHEP* **1112**, 115 (2011), arXiv:1110.3056 [physics.ins-det].

- [53] E. Aprile *et al.* (XENON), Astropart.Phys. **34**, 679₂₀₁₁
 (2011), arXiv:1001.2834 [astro-ph.IM].
- [54] E. Aprile *et al.* (XENON100), J.Phys. **G41**, 03520₂₀₁₃
 (2014), arXiv:1311.1088 [physics.ins-det].
- [55] L. Kastens *et al.*, Phys. Rev. C **80**, 045809 (2009).
- [56] A. Manalaysay, T. M. Undagoitia, A. Askin, L. Baudis₂₀₁₆
 A. Behrens, *et al.*, Rev.Sci.Instrum. **81**, 073303 (2010)₂₀₁₇
 arXiv:0908.0616 [astro-ph.IM].
- [57] R. L. Platzman, International Journal of Applied Radia₂₀₁₉
 tion and Isotopes **10**, 116 (1961).
- [58] C. E. Dahl, *The physics of background discrimination in liquid xenon, and first results from Xenon10 in the hunt for WIMP dark matter*, Ph.D. thesis, Princeton University (2009).
- [59] D. S. Akerib *et al.*, ArXiv e-prints (2015)₂₀₂₅
 arXiv:tritium.paper.
- [60] D. S. Akerib *et al.* (LUX Collaboration), ArXiv e-prints (2015), arXiv:dd.result.
- [61] B. Lenardo *et al.*, IEEE Trans.Nucl.Sci. **62**, 1 (2015).₂₀₂₉
- [62] F. Bezrukov, F. Kahlhoefer, and M. Lindner, Astroparticle Physics **35**, 119 (2011).
- [63] J. Thomas and D. A. Imel, Phys. Rev. A **36**, 614 (1987).
- [64] D. Mei *et al.*, Astroparticle Physics **30**, 12 (2008).
- [65] V. Y. Chepel *et al.*, Proceedings of the 1999 IEEE 13th International Conference on Dielectric Liquids , 52 (1999).
- [66] F. Arneodo *et al.*, Nucl. Inst. and Meth. A **449**, 147 (2000).
- [67] D. Akimov *et al.*, Phys. Lett. B **524**, 245 (2002).
- [68] E. Aprile *et al.*, Phys. Rev. D **72**, 072006 (2005).
- [69] A. Manzur *et al.*, Phys. Rev. C **81**, 025808 (2010).
- [70] G. Plante *et al.*, Phys. Rev. C **84**, 045805 (2011).
- [71] E. Aprile *et al.*, Phys. Rev. Lett. **97**, 081302 (2006).
- [72] C. Lee, *Mitigation of backgrounds for the Large Underground Xenon experiment*, Ph.D. thesis, Case Western Reserve University (2015).
- [73] J. D. Lewin and P. F. Smith, Astroparticle Physics **6**, 87 (1996).